Hybrid-Vlasov simulation of soft X-ray emissions at the Earth's dayside magnetospheric boundaries

M. Grandin[1]*, H. K. Connor[2], S. Hoilijoki[1], M. Battarbee[1], Y. Pfau-Kempf[1], U. Ganse[1], K. Papadakis[1], and M. Palmroth[1,3]

[1]Department of Physics, University of Helsinki, Helsinki, Finland;

[2]NASA Goddard Space Flight Center, Greenbelt, MD, 20771, USA;

[3]Space and Earth Observation Centre, Finnish Meteorological Institute, Helsinki, Finland

Key Points:

- We produce soft X-ray images of near-Earth space with a global hybrid-Vlasov simulation with southward interplanetary magnetic field.
- Flux transfer events can produce X-ray signatures despite being transient phenomena if they cumulatively increase the proton density locally.
- Mirror-mode structures in the magnetosheath can also produce soft X-ray signatures in time-integrated images.

Abstract: Solar wind charge exchange produces emissions in the soft X-ray energy range which can enable the study of near-Earth space regions such as the magnetopause, the magnetosheath and the polar cusps by remote sensing techniques. The Solar wind Magnetosphere Ionosphere Link Explorer (SMILE) and Lunar Environment heliospheric X-ray Imager (LEXI) missions aim to obtain soft X-ray images of near-Earth space thanks to their Soft X-ray Imager (SXI) instruments. While earlier modeling works have already simulated soft X-ray images as might be obtained by SMILE SXI during its mission, the numerical models used so far are all based on the magnetohydrodynamics description of the space plasma. To investigate the possible signatures of ion-kinetic-scale processes in soft X-ray images, we use for the first time a global hybrid-Vlasov simulation of the geospace from the Vlasiator model. The simulation is driven by fast and tenuous solar wind conditions and purely southward interplanetary magnetic field. We first produce global X-ray images of the dayside near-Earth space by placing a virtual imaging satellite at two different locations, providing meridional and equatorial views. We then analyze regional features present in the images and show that they correspond to signatures in soft X-ray emissions of mirror-mode wave structures in the magnetosheath and flux transfer events (FTEs) at the magnetopause. Our results suggest that, although the time scales associated with the motion of those transient phenomena will likely be significantly smaller than the integration time of the SMILE and LEXI imagers, mirror-mode structures and FTEs can cumulatively produce detectable signatures in the soft X-ray images. For instance, a local increase by 30% in the proton density at the dayside magnetopause resulting from the transit of multiple FTEs leads to a 12% enhancement in the line-of-sight- and time-integrated soft X-ray emissivity originating from this region. Likewise, a proton density increase by 14% in the magnetosheath associated with mirror-mode structures can result in an enhancement in the soft X-ray signal by 4%. These are likely conservative estimates, given that the solar wind conditions used in the Vlasiator run can be expected to generate weaker soft X-ray emissions than the more common denser solar wind. These results will contribute to the preparatory work for the SMILE and LEXI missions by providing the community with quantitative estimates of the effects of small-scale, transient phenomena occurring on the dayside.

Keywords: magnetosphere; magnetosheath; numerical simulation; SMILE; LEXI; soft X-ray emissions; hybrid-Vlasov model; polar cusp; flux transfer events; mirror-mode waves

1. Introduction

Over the past two decades, interest has grown in studying near-Earth space by observing the soft X-ray emissions created by

charge-exchange interactions between heavy, multiply charged ions and neutral species. For example, charge-exchange interactions between O^{7+} or O^{8+} ions present in the solar wind and neutral hydrogen atoms from the Earth's exosphere are known to lead to photon emissions through the de-excitation of the product ion species, which include photon energies in the soft X-ray range (0.5–0.7 keV). This process is known as solar wind charge

exchange (SWCX). A review by Sibeck et al. (2018) provides in-depth details on the processes at play as well as pioneering works on the study of terrestrial and planetary space through the observation of soft X-ray emissions.

Currently, several satellite missions aim at imaging near-Earth space in soft X-rays. Two major upcoming missions making use of SWCX soft X-ray imaging to reseach near-Earth space are the Lunar Environment heliospheric X-ray Imager (LEXI), led by Boston University in collaboration with NASA GSFC and several universities (http://sites.bu.edu/lexi), and the Solar wind Magnetosphere Ionosphere Link Explorer (SMILE) mission, designed jointly by the European Space Agency and the Chinese Academy of Sciences (Branduardi-Raymont et al., 2018). Both of these missions will provide soft X-ray images of the polar cusps and the magnetosheath, which are known to be the most prominent sources of SWCX soft X-ray emissions in near-Earth space, with a goal of understanding global interaction between the solar wind and the Earth's magnetosphere. After its expected launch in 2024, LEXI will observe the dayside magnetosheath from the lunar surface for up to two weeks of a short mission period due to the harsh lunar environment. SMILE will be launched in 2025 into a highly elliptical polar orbit with an apogee of ~20 Earth radii (R_E), observing the dayside magnetosheath and cusps for up to 40 continuous hours per orbit during three years of its mission period.

While there have been no wide-field-of-view soft X-ray observations of the geospace, the existence of near-Earth SWCX soft X-ray emissions has been studied in various works using data from the XMM and ROSAT astrophysics missions (e.g. Carter et al., 2010, 2011; Cravens et al., 2001; Snowden et al., 2004; Connor and Carter, 2019; Jung et al., 2022; Zhang YJ et al., 2022). Subsequently, modeling efforts were undertaken to understand the soft X-ray emissions detected by the ROSAT mission (Snowden et al., 1995) and to quantify the contributions of various source mechanisms (e.g., Cox, 1998; Cravens et al., 2001). Robertson and Cravens (2003b) were the first to produce images of the dayside magnetopause and magnetosheath in soft X-ray emissions through the SWCX mechanism using a numerical model, and based on their results they suggested that it might be possible to make use of those emissions to monitor the solar wind–magnetosphere interactions through remote sensing observations. The same authors also produced simulated images in soft X-rays for a virtual instrument placed on the Earth's surface and observing various directions in the sky (Robertson and Cravens, 2003a), and investigated the polar cusps' signatures in soft X-ray images in further simulations (Robertson et al., 2006).

More recent studies have taken up the modeling efforts as part of the preparatory phases of the LEXI and SMILE missions. Collier and Connor (2018) determined that the surface of the magnetopause could in principle be determined by soft X-ray imaging of near-Earth space, as the line-of-sight-integrated soft X-ray emissions maximize for observations tangential to the magnetopause surface. Based on these results, Sun TR et al. (2020) developed a tangent-fitting method to derive the magnetopause position in anticipated images from the Soft X-ray Imager (SXI) instrument onboard SMILE. Alternative methods to determine the magnetopause shape and position from SXI observations have been

devised by Wang C and Sun TR (2022). Among the processes taking place in near-Earth space and which could be studied using soft X-ray imaging, Sun TR et al. (2019) showed that SXI will be able to monitor the motions of the dayside magnetopause and of the polar cusps in response to changes in the solar wind driving conditions. Connor et al. (2021) also addressed similar research questions by simulating soft X-ray images which could be obtained during the SMILE and LEXI missions in an event when the interplanetary magnetic field (IMF) turns southward and an event when the solar wind density abruptly increases. They demonstrated that it might be possible to get information on the time variations in the magnetic reconnection rate at the dayside magnetopause using such remote-sensing techniques, and they argued that these missions could enable the tracing of the energy flow from the solar wind all the way to the cusps with the same instrument.

The above-mentioned modeling studies all used numerical models of space plasma based on the magnetohydrodynamics (MHD) paradigm, which treats the plasma as a fluid. To complement the results obtained with this approach, it would be interesting to carry out modeling studies of SWCX soft X-ray imaging based on a global model of near-Earth space relying on a kinetic description of the plasma. Indeed, a certain number of space plasma processes are intrinsically of kinetic origin, and therefore cannot emerge in MHD simulations. Examples of such processes include the growth of instabilities, wave–particle interactions as well as ion-scale physics associated with magnetic reconnection.

In this paper, we will for the first time carry out a study of soft X-ray emissions relying on a 3D global hybrid-Vlasov simulation. We will make use of the kinetic nature of the model to investigate to what extent near-Earth space processes associated with ion-scale physics might produce signatures in soft X-ray images as will be obtained by the SMILE SXI instrument. To that aim, we will make use of Vlasiator (Palmroth et al., 2018), which is a global hybrid-Vlasov model of near-Earth space. In particular, we will quantify the signatures in terms of line-of-sight- and time-integrated soft X-ray emissions of two transient phenomena occurring on the dayside: mirror-mode waves in the magnetosheath and flux transfer events (FTEs) produced by magnetic reconnection at the dayside magnetopause. Mirror-mode waves are generated by temperature anisotropy in the magnetosheath and appear as nonpropagating structures (in the plasma frame) with anticorrelated variations in plasma density and magnetic field magnitude (Hasegawa, 1969). FTEs are flux-rope-like structures forming along the dayside magnetopause in presence of multiple or bursty reconnection lines associated with southward IMF conditions, which often form near the subsolar point and propagate toward the polar cusps (Russell and Elphic, 1978; Rijnbeek et al., 1984; Berchem and Russell, 1984).

The paper is organized as follows. The Vlasiator model and the methodology to construct soft X-ray images in the utilized simulation run are introduced in Section 2. Then, in Section 3, we present examples of global images of the dayside near-Earth space obtained with virtual imaging spacecraft placed at two locations: on the dawnside (meridional view) and above the north pole (equatorial view). Section 4 describes the analysis and results

on the detectability of transient processes (FTEs and mirror-mode waves) in the simulated soft X-ray images. A discussion of the results is provided in Section 5, and Section 6 gives a summary of the main conclusions of the paper.

2. Models and Methods

2.1 Vlasiator

2.1.1 Model

Vlasiator (von Alfthan et al., 2014; Palmroth et al., 2018) is a global hybrid-Vlasov code simulating near-Earth plasma at ion-kinetic scales. In the hybrid-Vlasov approach, ions are described through their velocity distribution function (VDF) which is discretized in a 3-dimensional (3D) velocity grid, resulting in ion populations evolving in a 6D phase space (3D in ordinary space + 3D in velocity space). In practice, Vlasiator solves the Vlasov equation for ions and treats electrons as a massless, charge-neutralizing fluid. While most existing Vlasiator simulation runs consider protons as the sole ion species, heavier ions such as He^{2+} have also been included in a few runs (e.g., Battarbee et al., 2020a).

Electromagnetic fields are propagated in time by solving Maxwell's equations under the Darwin approximation, i.e., neglecting the displacement current term in Ampère's law. The equation system is closed through a generalized Ohm's law including the Hall term and a polytropic (adiabatic) description of the electron pressure gradient term. The model considers an ideal geomagnetic dipole field using a nonscaled strength 8×10^{15} T m^3 and with a zero tilt between its axis and the Z direction in the Geocentric Solar Ecliptic (GSE) frame of reference — in the GSE frame, the Earth's center is at the origin, the X axis points toward the Sun, the Z axis toward the north, and the Y axis completes the orthonormal frame and points toward dusk. The geomagnetic dipole is described through a vector potential, which is scaled to zero at the inflow boundary in order to prevent magnetic divergence entering the simulation domain. Magnetic and electric fields are propagated using a finite difference upwind field solver (Londrillo and del Zanna, 2004).

The simulation domain extent varies from one run to another, but it generally includes the dayside magnetosphere, the magnetosheath, the bow shock, the ion foreshock (if driving conditions allow for its existence), and part of the magnetotail. This has allowed for a great variety of studies focusing on a wide range of processes, such as foreshock waves (Turc et al., 2018), foreshock cavitons (Tarvus et al., 2021), bow shock nonlocality (Battarbee et al., 2020b), magnetosheath waves (Hoilijoki et al., 2016; Dubart et al., 2020), energy transfer across the magnetopause (Ala-Lahti et al., 2022), magnetotail current sheet flapping (Juusola et al., 2018), or auroral proton precipitation (Grandin et al., 2019, 2020). While those past studies were based on 2D–3V runs (2D in ordinary space, 3D in velocity space), recent code developments have enabled the production of the first Vlasiator 3D–3V runs. This study makes use of one such 3D–3V run, described below.

2.1.2 Simulation run

The Vlasiator run used in this study has its simulation domain extending from $-110\,R_E$ to $50\,R_E$ in the X direction (with R_E the Earth's radius; $R_E = 6371$ km) and confined within $|Y| < 58\,R_E$ and $|Z| < 58\,R_E$. The inner boundary lies at $4.7\,R_E$ from the origin; it is implemented as a perfectly conducting sphere on which VDFs are fixed Maxwellian distributions. External boundaries have Neumann boundary conditions, except for the $+X$ wall from which the solar wind and IMF enter the simulation domain.

Driving conditions in this 3D–3V run are as follows: purely southward IMF with $B_x = B_y = 0$ and $B_z = -5$ nT, solar wind with proton number density of 1 cm^{-3}, speed along the $-X$ direction at 750 km s^{-1}, temperature of 500 K. Solar wind conditions are homogeneous and constant throughout the simulation. Protons are the sole ion species in this run. Initial conditions are such that the whole simulation domain is filled with solar-wind-like Maxwellian VDFs and the superposition of the dipole geomagnetic field with the IMF, and the near-Earth space regions thus form self-consistently during the first few hundred seconds of the simulation. In this study, we will focus on the time interval starting at $t = 800$ s, when the dayside magnetosphere is well formed and lasting until the end of the simulation at $t = 1506$ s. In this run, an output file was written at a cadence of 1 s, which contains the plasma bulk parameters as well as electromagnetic field components in every simulation cell.

One development which made 3D–3V runs possible was the implementation of adaptive mesh refinement (AMR) for the ordinary-space mesh. In this run, least-refined regions have a base grid with 8000 km resolution, and there are three refinement levels at 4000, 2000 and 1000 km resolution to improve the description of regions of interest where ion-scale kinetic processes are important (bow shock, magnetosheath, magnetopause, magnetotail current sheet). At such resolutions, one expects that some of the kinetic processes cannot arise, as the ion inertial length is not resolved. For instance, the ion cyclotron instability cannot grow with such a coarse grid, hence most of the free energy associated with unstable ion distributions will feed the mirror instability (Dubart et al., 2020). Nevertheless, as will be seen in the upcoming sections, the general morphology of the near-Earth space regions and the plasma parameter values are realistic, making this run usable for the purpose of this study. The velocity space is a uniform 3D Cartesian grid with a resolution of 40 km s^{-1}. In the solar wind, the Alfvén speed is 109 km s^{-1} and the thermal speed is 111 km s^{-1}, and in regions of near-Earth space which are hotter or have a stronger magnetic field, these characteristic speeds are larger, ensuring that the associated physical processes are resolved in a satisfactory way in the regions of interest. The electric and magnetic fields are solved on a uniform Cartesian grid at constant resolution of 1000 km in a process described by Papadakis et al. (2022).

Figure 1 gives an overview of the simulation domain at $t = 1100$ s. It consists of three slices in the $X = 0$, $Y = 0$ and $Z = 0$ planes showing the proton number density. While the chosen viewing angle and slice extents enable seeing dayside structures and processes relevant to this study, the actual simulation domain extends beyond this figure (see above). In the figure, one can identify the bow shock, the magnetosheath exhibiting wave-like structures, the magnetopause as well as the northern polar cusp. The magnetotail, partly hidden behind the $X = 0$ slice, will not be the focus of
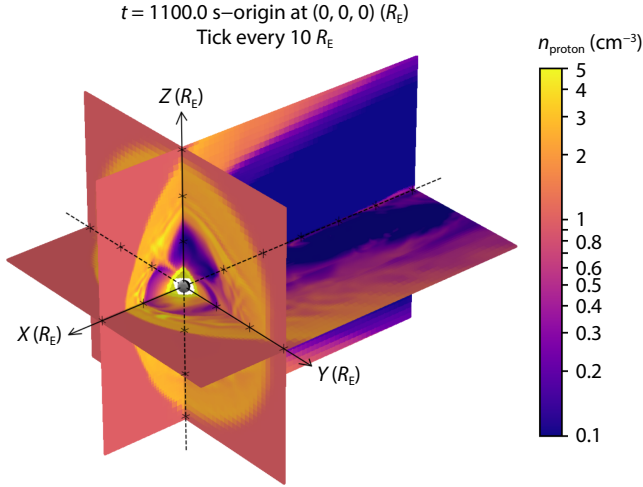
$t = 1100.0$ s−origin at $(0, 0, 0)$ (R_E)
Tick every 10 R_E

n_{proton} (cm^{-3})

Figure 1. Proton number density in the $X = 0$, $Y = 0$ and $Z = 0$ planes of the simulation domain at $t = 1100$ s in the Vlasiator simulation, wherein the bow shock, the magnetopause and the northern polar cusp are prominent. One can also identify wave-like structures in the dayside magnetosheath.

this study but exhibits complex dynamics.

2.2 Soft X-ray Image Generation

2.2.1 Analytical expression of soft X-ray emissivity

In this study, the method to derive the local soft X-ray emissivity within the simulation will follow the same approach as past studies (e.g. Connor et al., 2021; Sun TR et al., 2020). It is calculated at position $\boldsymbol{r}$ in the simulation domain with the following expression

$$Q_{loc}(\boldsymbol{r}) = \frac{\alpha_X}{4\pi} n_p(\boldsymbol{r}) n_H(\boldsymbol{r}) V_{eff}(\boldsymbol{r}), \qquad (1)$$

where α_X is the interaction efficiency factor, n_p is the proton number density, n_H is the neutral hydrogen atom density, and V_{eff} is the so-called "effective velocity", defined as

$$V_{eff}(\boldsymbol{r}) = \sqrt{V_p(\boldsymbol{r})^2 + \frac{5}{3} \frac{k_B T(\boldsymbol{r})}{m_p}}. \qquad (2)$$

In Equation (2), V_p is the proton bulk velocity, k_B is Boltzmann's constant, T is the plasma temperature, and m_p is the proton mass. This equation expresses V_{eff} in m·s^{-1}. Note that protons do not emit soft X-rays. The highly charged, heavy solar wind ions like C^{6+}, N^{6+}, N^{7+}, Ne^{9+}, S^{10+}, O^{7+}, and O^{8+} emit soft X-rays through SWCX (Sibeck et al., 2018). By multiplying by the interaction efficiency factor α_X, the proton-based quantity in Equation (1) is transformed into the soft X-ray emissivity caused by the source ions.

Since Vlasiator does not simulate the exosphere, we use the analytical model from Cravens et al. (2001) for the neutral density, given as

$$n_H(\boldsymbol{r}) = 25 \left(\frac{10 R_E}{r} \right)^3, \qquad (3)$$

with r the distance of the considered location to the Earth's center. The above expression gives n_H in cm^{-3}, and in the continuation of the study, we will express soft X-ray emissivity quantities using centimeter as the unit of length, following the common usage for

this specific application. For instance, Q_{loc} will be expressed in keV cm^{-3} s^{-1} sr^{-1}. In this study, we will use an interaction efficiency factor value of $\alpha_X = 1 \times 10^{-15}$ eV cm^2, following Sun TR et al. (2019) and references therein.

2.2.2 Line-of-Sight integration from a virtual spacecraft

In order to simulate soft X-ray images close to as they would be obtained by a spacecraft such as LEXI and SMILE, we place a virtual spacecraft in the Vlasiator simulation domain and calculate the line-of-sight-integrated value of the local soft X-ray emissivity along multiple viewing directions within the instrument field-of-view, which corresponds to as many pixels in the images. We define this quantity $Q_{int}(\varphi, \lambda)$ as a function of the azimuth φ and elevation λ of a given line of sight.

$$Q_{int}(\varphi, \lambda) = \int Q_{loc}(l_{\varphi,\lambda}) \, dl_{\varphi,\lambda}, \qquad (4)$$

with $l_{\varphi,\lambda}$ the distance from the spacecraft along the line of sight associated with the (φ, λ) azimuth–elevation pair. By convention, we will have the $(0, 0)$ pair corresponding to the direction toward the Earth's center. The obtained instantaneous line-of-sight emissivity Q_{int} will be given in keV cm^{-2} s^{-1} sr^{-1} in this study.

Soft X-ray images simulated using this Vlasiator run will have an angular resolution of 0.33° in both azimuth and elevation, and the line-of-sight integration will take place between the virtual satellite location and the outer boundary of the simulation domain. If a given line of sight intersects the inner boundary, Q_{int} will not be calculated. The virtual spacecraft will be placed either at $(0, -30 R_E, 0)$ in GSE coordinates (i.e., observing from the dawnside) or at $(0, 0, 30 R_E)$ (i.e., observing from above the north pole). The two virtual satellites are selected to provide the side and polar views of the Earth's magnetosphere similar to LEXI and SMILE, respectively, while keeping the radial distances fixed at 30 R_E between the apogees of LEXI and SMILE for easy comparison of soft X-ray signatures in polar and side views. Both instantaneous values of Q_{int} and time-integrated ones over 300 s, Q_{int_300s}, will be shown, as the latter correspond to the integration time that SMILE and LEXI soft X-ray imagers require for good signal-to-noise ratios (Branduardi-Raymont et al., 2018; Connor et al., 2021).

3. Simulated Soft X-ray Images

In this section, we present the simulated soft X-ray images obtained from the Vlasiator run when the virtual imaging spacecraft is viewing the dayside magnetosphere either from the dawnside or from above the north pole. We first show instantaneous images alongside relevant plasma parameters in the noon–midnight meridional plane or equatorial plane, respectively. Animations showing such instantanous images every second from $t = 800$ s to $t = 1506$ s are provided in supplementary material. We then time-integrate these instantaneous images during three 300 s time intervals and discuss the main features that can be observed.

3.1 Instantaneous Simulated Soft X-ray Images

3.1.1 View from dawn

Figure 2 shows plasma parameters in the noon–midnight meridional plane $(Y = 0)$ at $t = 1100$ s in the simulation. Figure 2a displays the proton number density, in which the magnetosheath

and the polar cusps stand out. One can identify the bow shock, whose subsolar point lies approximately at 15 R_E. Given the purely southward IMF orientation, the bow shock is essentially quasi-perpendicular, which is why no ion foreshock is present. Within the magnetosheath, density irregularities are particularly prominent. We will show in Section 4.2 that these correspond to mirror-mode waves. The magnetopause subsolar point lies at about 10 R_E.

Figure 2b gives the proton bulk velocity. When crossing the bow shock, the solar wind slows down from its inflow speed of 750 km s^{-1} to velocities on the order of 200–300 km s^{-1}. We can see that plasma convection at the dayside magnetopause gets faster at higher latitudes, before slowing down again when the plasma reaches the polar cusps.

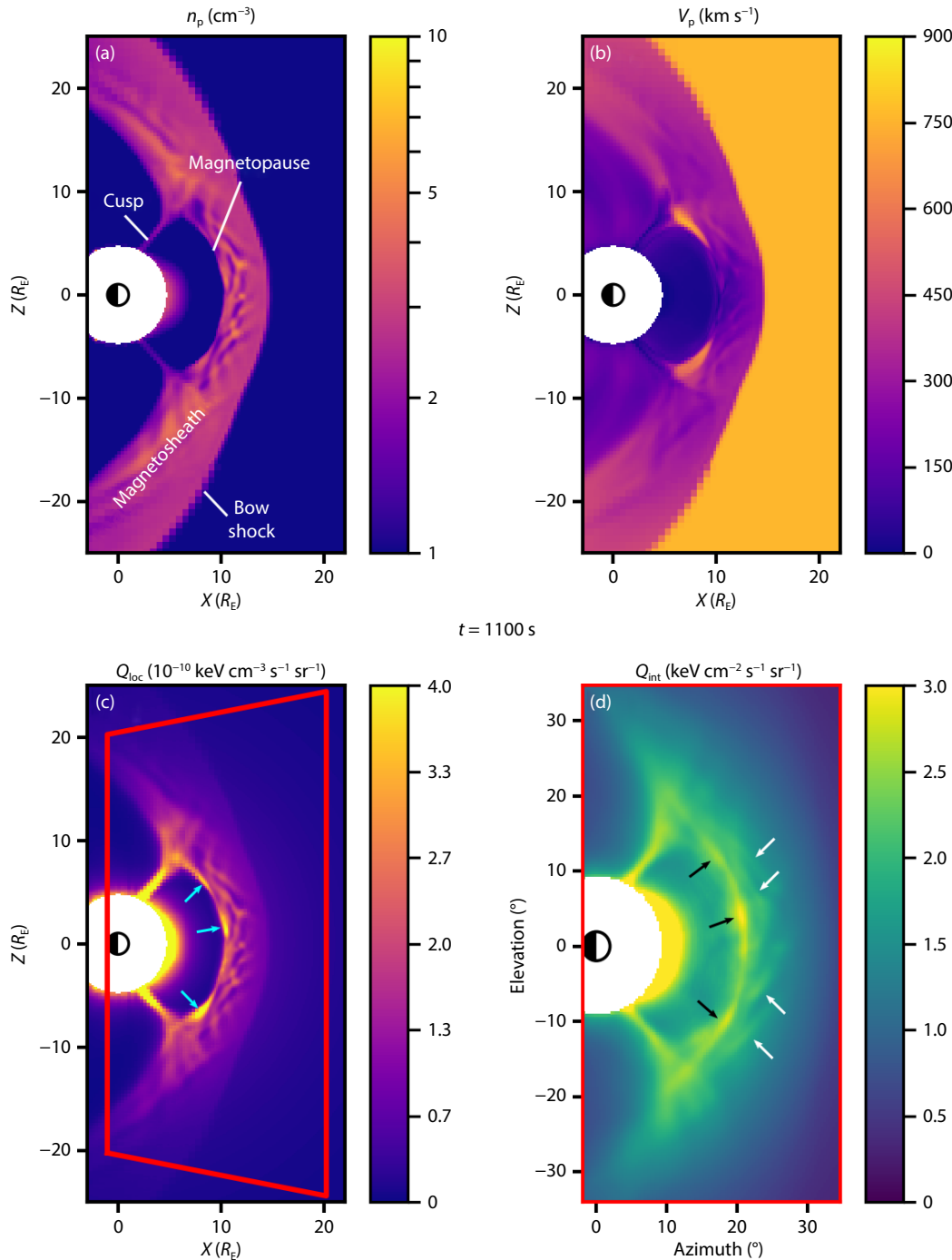Figure 2c presents the local soft X-ray emissivity in the plane, Q_{loc}

Figure 2. (a) Proton number density, (b) proton bulk velocity, and (c) local soft X-ray emissivity in the $Y = 0$ plane at $t = 1100$ s. (d) Instantaneous soft X-ray image with 1 s integration time from a virtual spacecraft placed at (0, −30 R_E, 0) at t=1100 s. The cyan arrows in panel (c) indicate flux transfer event signatures in soft X-rays, and the red trapezoid indicates the intersection of the instrument's field of view shown in panel (d) with the $Y = 0$ plane. The black and white arrows in panel (d) indicate structures discussed in the text.

Grandin M et al.: Vlasiator simulation of solar wind charge exchange soft X-ray emissions

(calculated with Equation (1)), which depends not only on the previous two parameters (n_p and V_p), but also on the plasma temperature and the neutral density, not shown in the figure. The most prominent features in Q_{loc} are the polar cusps and the magnetosheath, with values reaching 4×10^{-10} keV cm^{-3} s^{-1} sr^{-1}. In the magnetosheath, the wave field is particularly visible. Brighter areas along the dayside magnetopause can also be identified (indicated with cyan arrows); we will show in Section 4.1 that these are flux transfer events (FTEs), which appear as regions of slightly enhanced proton density in Figure 2a.

Figure 2d shows the instantaneous image of line-of-sight-integrated soft X-ray emissions, Q_{int}, viewed from a virtual imaging satellite placed at (0, −30 R_E, 0), at this same time. Due to the geometry associated with the setup, the field of view associated with this image intersects the noon–midnight meridional plane within the red trapezoid in Figure 2c. Elevation is the angle along the Z direction, whereas azimuth is along X. In this instantaneous image, the brightest areas correspond to the cusps and the magnetopause, with values of Q_{int} on the order of 3 keV cm^{-2} s^{-1} sr^{-1}. The cusps are particularly bright because they have a high density of neutrals (see Equation (3)). It was shown in previous studies that lines of sight with maximum brightness correspond to directions tangential to the magnetopause (Collier and Connor, 2018). The very bright area close to the inner boundary is caused by boundary effects, as proton density is elevated at low latitudes near the inner boundary (Figure 2a), due to leakage of cold plasma resulting from the boundary condition. However, the bright SWCX soft X-ray emission near the inner boundary does not exist in reality and is an artificial effect by calculating soft X-ray emissivity based on proton parameters Equation (1).

In the instantaneous image of Q_{int}, one can notice signatures likely associated with the wave field in the magnetosheath (indicated with white arrows), as well as brighter spots along the dayside magnetopause (indicated with black arrows). This means that, despite the line-of-sight integration and parallax effects, some of the structures identified in Q_{loc} (Figure 2c) also show in Q_{int}. The possible relation between such structures and transient processes will be investigated in Section 4.

An animated version of Figure 2 is provided in the supplementary material as Movie S1. In this animation, we can especially visualize how the magnetosheath wave signatures and dayside magnetopause bright spots move as a function of time. The fact that the latter are colocated with confined regions of increased proton density forming near the subsolar point and transiting along the magnetopause toward the polar cusps strongly suggests that these are signatures of FTEs (see Section 4.1 and discussion in Section 5).

3.1.2 View from north
Figure 3 is analogous to Figure 2, but this time the virtual imaging spacecraft has been placed above the north pole, at (0, 0, 30 R_E) in GSE coordinates. The chosen time step for this instantaneous snapshot of plasma parameters and soft X-ray emissions is $t = 1100$ s, like previously. Figures 3a–c show parameters in the equatorial plane ($Z = 0$), and Figure 3d shows the line of sight-integrated soft X-ray emissions as a function of azimuth (along the

X direction) and elevation (this time along Y).

The bow shock and dayside magnetopause are again prominent in the proton density panel (Figure 3a), as are the magnetosheath waves. The proton bulk velocity panel indicates the abrupt decrease in velocity across the bow shock, while the magnetosheath plasma accelerates once it reaches the flanks (Figure 3b). In local soft X-ray emissivity (Figure 3c), it is again the magnetosheath that shows up the most (ignoring the artifacts near the inner boundary).

In the instantaneous soft X-ray emission image (Figure 3d), a bright arc is visible across elevations, corresponding to the dayside magnetopause observed tangentially. Beyond the magnetopause signature, one can also see elongated structures originating from the magnetosheath. Due to the viewing angle, polar cusps are not visible in this image. Like in Figure 2, the bright emissions near the inner boundary are associated with boundary effects and would not be present in nature. An animated version of Figure 3 is provided in the supplementary material as Movie S2. In this animation, we can see how the elongated magnetosheath structures drift Earthward until they merge with the magnetopause signature, which occasionally brightens and exhibits undulations (e.g., around $t = 1000$ s and $t = 1440$ s).

3.2 Time-Integrated Soft X-ray Images

3.2.1 View from dawn
While the instantaneous soft X-ray images presented above show many interesting features, they do not correspond to images which could be obtained by SMILE and LEXI, as the instruments will need an integration time on the order of 300 s to obtain a sufficient number of counts. We therefore produce time-integrated images over three 300 s time intervals during the studied part of the simulation. We first consider the view from a virtual imaging spacecraft in the dawn sector; Figure 4 shows time-integrated soft X-ray images obtained during $t = 800–1100$ s (Figure 4a), $t = 950–1250$ s (Figure 4b), and $t = 1100–1400$ s (Figure 4c). In these images, the brightest structures correspond to the cusps as well as the dayside magnetopause.

It is clear from the figures that the time integration blurs out most small-scale structures that are associated with transient phenomena at the magnetopause and in the magnetosheath. However, one can see some irregularity in the shape and brightness of the magnetopause signature, such as a dimmer and thinner region at elevations near −3° in Figure 4a, and also at elevations near −7° in Figure 4c, for instance (indicated with black arrows). Conversely, parts of the dayside magnetopause signature appear brighter, like regions near +3° and −9° elevations in Figure 4a (indicated with white arrows). We will investigate the possible connection between these brighter Q_{int_300s} values at the dayside magnetopause and FTEs in Section 4.1.

Besides, Figures 4b–c exhibit brighter stripes in their magnetosheath signatures (indicated with magenta arrows). Such stripes have oblique orientations with respect to the Earth–Sun line and can be seen in both the northern and the southern part of the domain. In Section 4.2, we will show that these signatures are likely the result of mirror-mode waves in the magnetosheath.
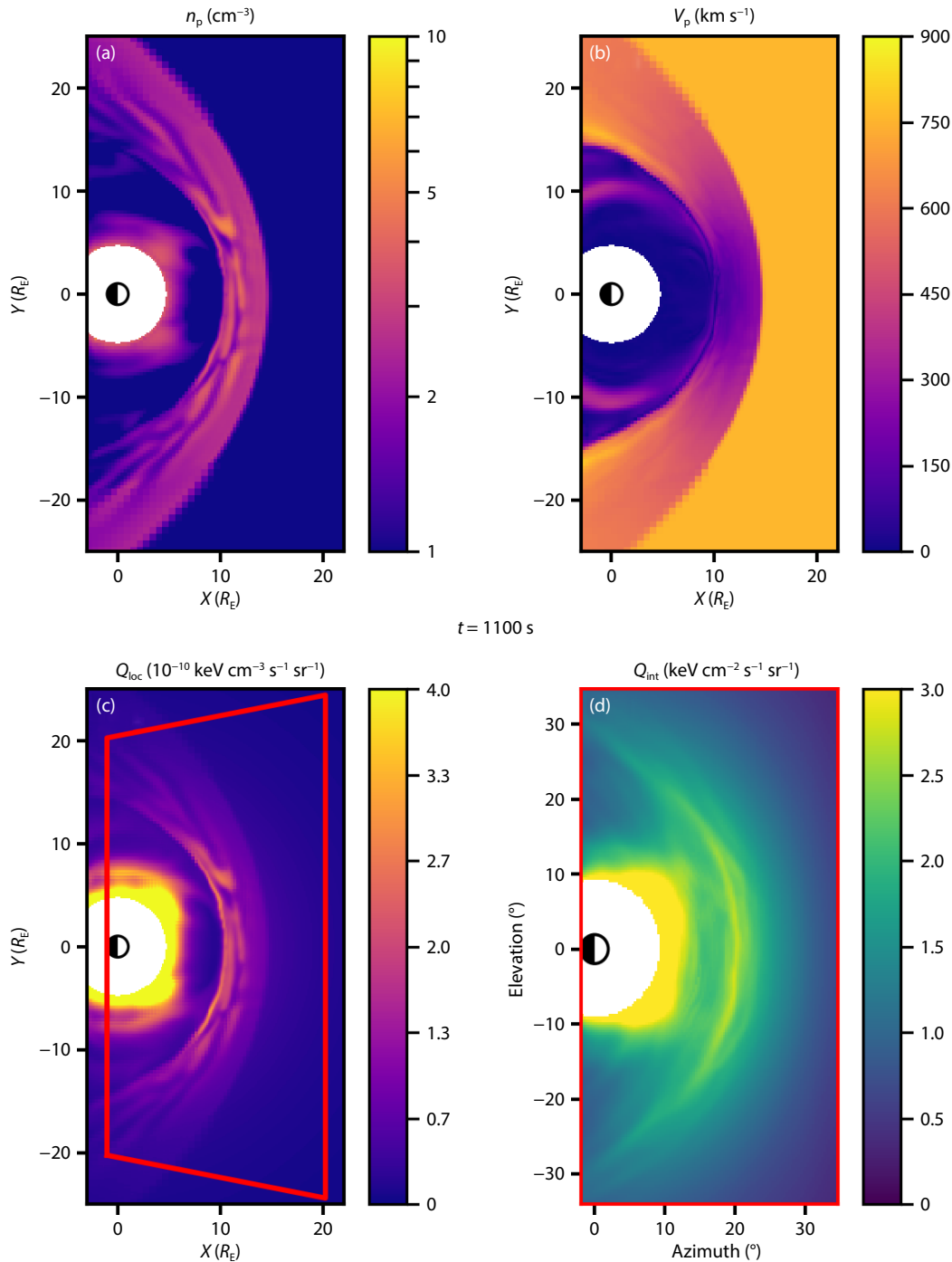
Figure 3. (a) Proton number density, (b) proton bulk velocity, and (c) local soft X-ray emissivity in the $Z = 0$ plane at $t = 1100$ s. (d) Instantaneous soft X-ray image with 1 s integration time from a virtual spacecraft placed at $(0, 0, 30\,R_E)$ at $t = 1100$ s. The red trapezoid in panel (c) indicates the intersection of the instrument's field of view shown in panel (d) with the $Z = 0$ plane.

In order to better visualize differences between the three images, we will look at Q_{int_300s} values along a few selected cuts. Figure 5a reproduces the time-integrated image within $t = 950–1250$ s (i.e., Figure 4b) and indicates where five cuts have been performed, along which the Q_{int_300s} values are extracted and displayed in Figures 5b–f for the three time intervals.

Figures 5b and 5c show time-integrated soft X-ray emission values along the black and grey straight lines, respectively, which both cut across the magnetopause and through the magnetosheath.

The horizontal axis is the angular distance, noted d, of a point on the line from the $(0, 0)$ viewing direction (calculated as $\sqrt{\varphi^2 + \lambda^2}$). In both panels, Q_{int_300s} peaks at $d \approx 21°$, which corresponds to the tangent direction to the magnetopause. While the curves corresponding to the three integrating time intervals are almost perfectly superimposed on top of each other in Figure 5b, one can see that the peak was slightly reduced and drifted to larger d values with time in Figure 5c. Around $d \approx 24°$, there are small-amplitude fluctuations visible in the violet and orange curves, in

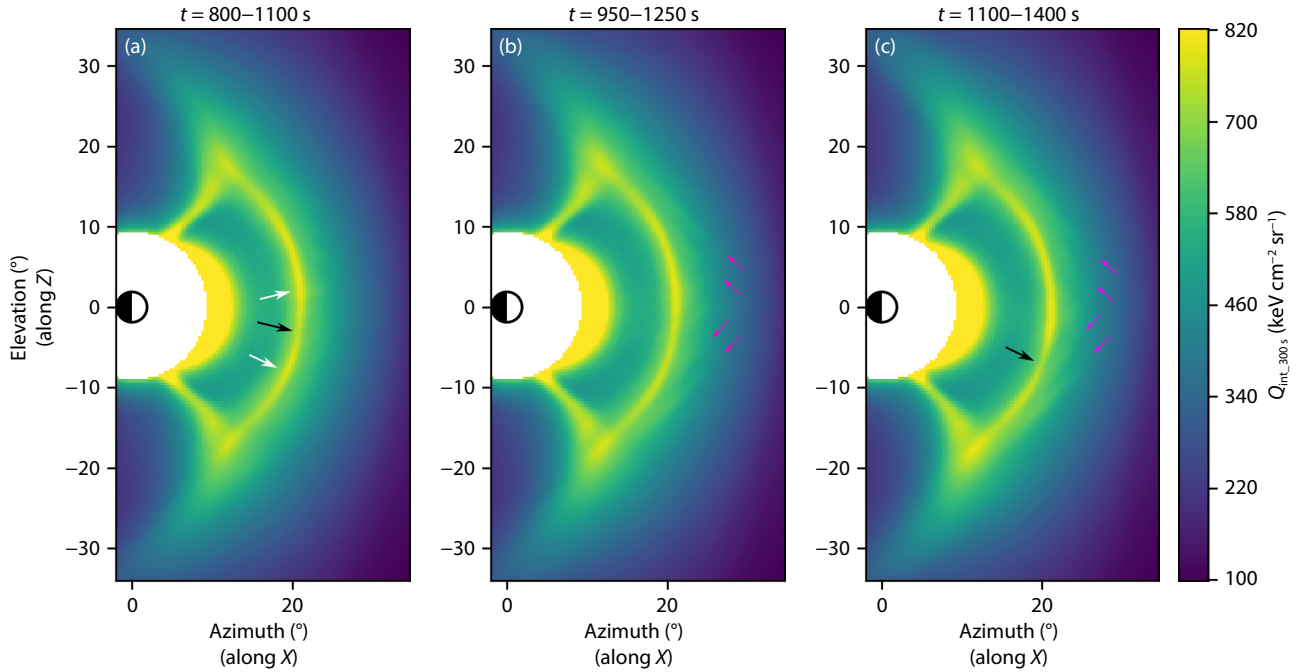**Grandin M et al.: Vlasiator simulation of solar wind charge exchange soft X-ray emissions**

Figure 4. Soft X-ray image obtained from a virtual spacecraft located at $(0, -30\,R_E, 0)$ with 300 s integration time starting at (a) $t = 800$ s, (b) $t = 950$ s, and (c) $t = 1100$ s in the simulation.
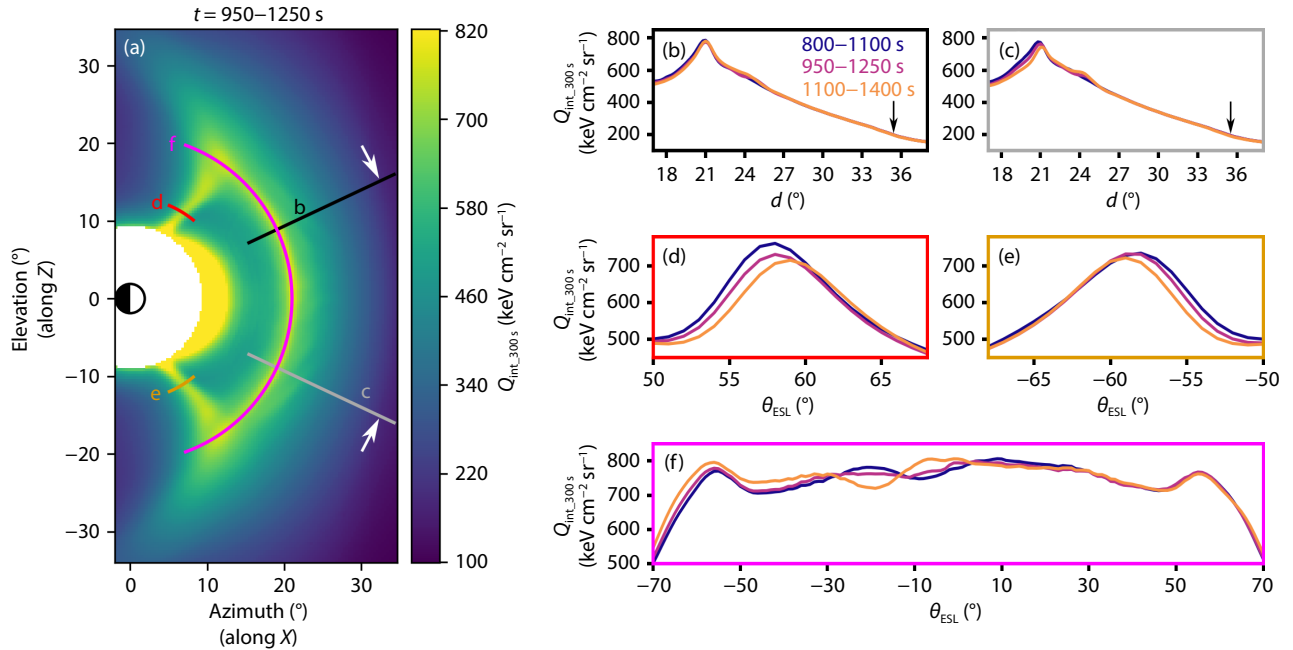

Figure 5. (a) Time-integrated soft X-ray image from $t = 950$ to $t=1250$ s obtained from a virtual spacecraft located at $(0, -30\,R_E, 0)$ (same as Figure 4b), with several cuts along and across boundary region signatures. (b) Soft X-ray emission along the black cut through the northern-hemisphere magnetopause and magnetosheath signatures. (c) Same along the grey cut through the southern-hemisphere magnetopause and magnetosheath signatures. (d) Same along the red cut across the northern cusp signature. (e) Same along the orange cut across the southern cusp signature. (f) Same along the magenta cut following the dayside magnetopause signature. In panels (b–f), the three lines correspond to the three studied 300 s time intervals for image acquisition.

both panels, corresponding to the stripes identified in Figures 4b–c. A last observation that can be made from these two panels is a change in the slope of Q_{int_300s} occurring at $d \approx 35.5°$, indicated with black arrows. The slope changes from about -27 to -17 keV cm^{-2} sr^{-1} deg^{-1}. This transition takes place when the line

of sight becomes tangent to the (quasi-perpendicular) bow shock, as shown in Fig. 4 of Connor et al. (2021). The corresponding locations in Figure 5a are indicated with white arrows.

Values of Q_{int_300s} along the red and orange curved lines, cutting

Grandin M et al.: Vlasiator simulation of solar wind charge exchange soft X-ray emissions

through the northern and southern cusp, respectively, are shown in Figures 5d and 5e. The horizontal axis is the angle between the Earth–point direction and the Earth–Sun line, noted θ_{ESL}. In both hemispheres, the cusp signature drifted slightly poleward with time, although the differences are relatively small.

Figure 5f give the Q_{int_300s} values along the magenta curve, which essentially follows the magnetopause signature in the images, as a function of θ_{ESL}. It shows quite clearly the variations in Q_{int_300s} previously identified in Figure 4 and enables estimating the amplitude of those variations, which can reach up to 90 keV cm^{-2} sr^{-1} (orange curve peak-to-trough amplitude at θ_{ESL} within [−20°, −10°]), i.e. representing about 10% of the average value. Other peaks can be identified at $\theta_{ESL} \approx \pm 55°$, corresponding to locations in the high-altitude polar cusps.

3.2.2 View from north

By applying the same methodology as above, we can also produce time-integrated soft X-ray images as would be obtained from the virtual imaging spacecraft placed above the north pole. Figure 6 presents the three images corresponding to the same integration intervals (i.e, $t = 800–1100$ s, $t = 950–1250$ s, and $t = 1100–1400$ s).

In the three panels, the brightest signature comes from the dayside magnetopause, with brightness maximizing at locations corresponding to low nose angles and signatures becoming fainter toward the flanks of the magnetopause. Magnetosheath stripes also show from this perspective, and are visible in all three panels (indicated with magenta arrows), with mostly oblique orientations. Beyond the magnetopause signature near the flanks, a second, fainter line parallel to it can be seen, especially in Figures 6b–c (indicated with black arrows). This parallel line might be associated with the same processes as the stripes closer to the subsolar point, as they appear similar in terms of brightness and orientation.

Figure 7 shows the values of Q_{int_300s} along a few selected cuts, in a same way as in Figure 5. Figure 7a reproduces Figure 5b and indicates where three cuts are considered to study the variations of Q_{int_300s} along the magnetopause X-ray signature as well as across the magnetosheath in the pre-noon and post-noon sectors.

We can see from Figures 7b–c that, along the cuts crossing the magnetosheath, the integrated soft X-ray emissivity peaks at $d \approx 21°$ in both the post-noon and pre-noon sectors, respectively, with a slight reduction in the peak value. Sunward from the peak (i.e. at larger d values), fluctuations in Q_{int_300s} can be seen, almost reaching a secondary peak at $d \approx 23°$ (more visible in the dawnside cut, Figure 7c). This corresponds to the oblique stripes indicated with magenta arrows in Figure 6.

Finally, looking at Q_{int_300s} values along the magenta cut following the magnetopause signature (Figure 7d), we note that the signal roughly follows linear slopes in the flanks ($|\theta_{ESL}| > 30°$), with little to no evolution with time. On the other hand, the section corresponding to the nose of the magnetopause exhibits fluctuations and variability amounting to about 5% of the Q_{int_300s} values (up to 40 keV cm^{-2} sr^{-1} between the violet and the orange lines at $\theta_{ESL} \approx -20°$). In a given image (i.e., focusing on a single line in Figure 7d), fluctuations can lead to the appearance of several local maxima in Q_{int_300s}, denoting the existence of structures near the magnetopause nose. These structures might be associated with the nature of the reconnection taking place at the dayside magnetopause, which can either be over an extended X-line or on the contrary more patchy (Walsh et al., 2017; Atz et al., 2022).

4. Signatures of Transient Processes in Soft X-ray Images

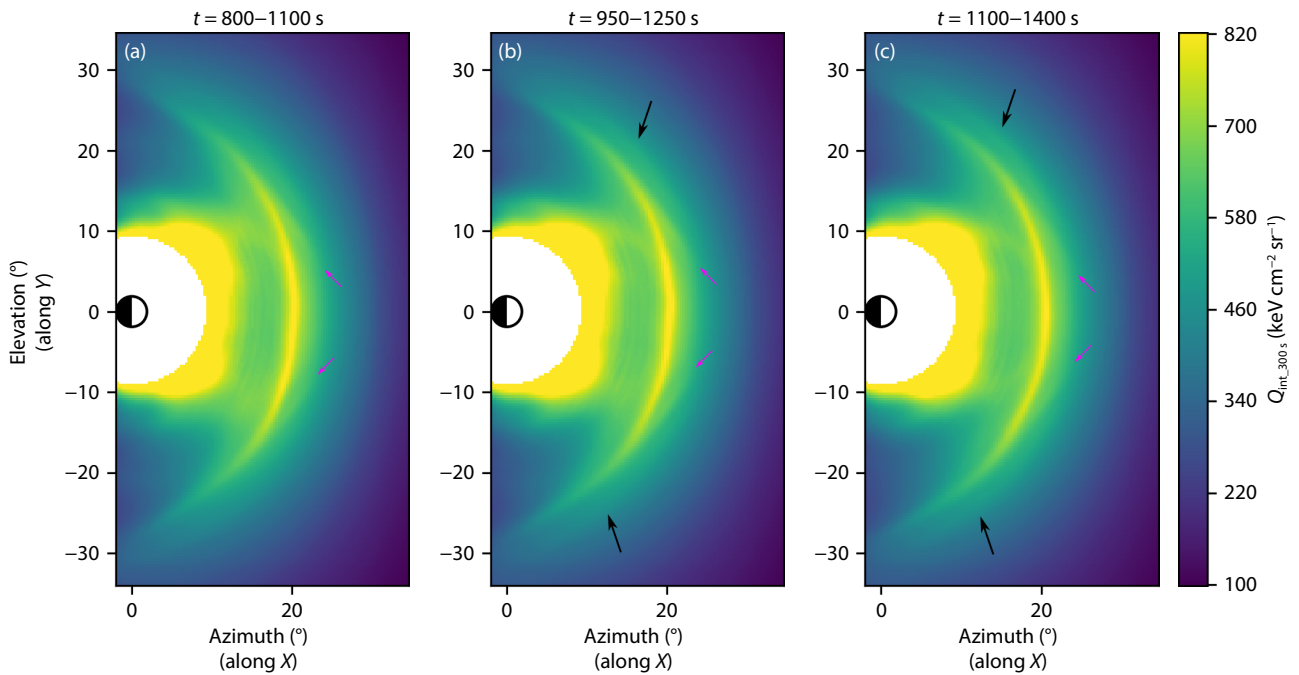In this section, we will investigate to what extent transient

Figure 6. Same as Figure 4 but with the virtual spacecraft placed at (0, 0, 30 R_E).

Grandin M et al.: Vlasiator simulation of solar wind charge exchange soft X-ray emissions
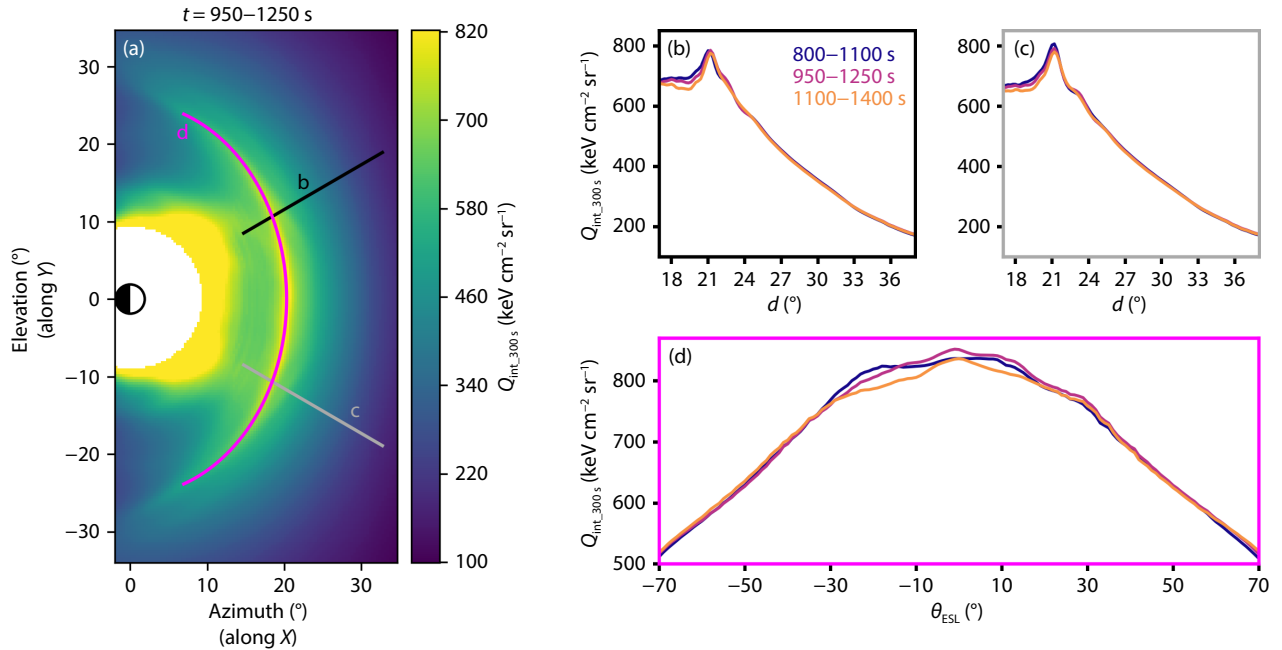
Figure 7. (a) Time-integrated soft X-ray image from $t = 950$ to $t = 1250$ s obtained from a virtual spacecraft located at $(0, 0, 30\,R_E)$ (same as Figure 6b), with several cuts along and across boundary region signatures. (b) Soft X-ray emission along the black cut through the post-noon magnetopause and magnetosheath signatures. (c) Same along the grey cut through the pre-noon magnetopause and magnetosheath signatures. (d) Same along the magenta cut following the dayside magnetopause signature. In panels (b–d), the three lines correspond to the three studied 300 s time intervals for image acquisition.

processes taking place in the magnetosheath and at the dayside magnetopause can induce signatures in soft X-ray images as will be measured by SMILE and LEXI SXI. We will focus on two processes: flux transfer events forming by magnetic reconnection at the dayside magnetopause and mirror-mode waves developing in the magnetosheath.

4.1 Flux Transfer Events at the Magnetopause

In Vlasiator 2D–3V runs driven by IMF with a southward B_z component, flux transfer events regularly form at the magnetopause near the subsolar point (Hoilijoki et al., 2017, 2019), and they propagate poleward toward the cusps, with consequences in terms of energy transfer into the magnetosphere (Ala-Lahti et al., 2022) and proton precipitation into the cusps (Grandin et al., 2020).

In this 3D–3V run, FTEs also form near the subsolar point and gradually follow the magnetopause toward the cusps, in both hemispheres. This can be seen in Supplementary Movie S3, where FTEs appear as regions of increased proton density enclosed within a magnetic island. To investigate whether these FTEs can have a signature on soft X-ray images, we first find a simple way to detect and track them along the dayside magnetopause, and we then look at their time-integrated parameters over 300 s windows.

Figure 8a shows (background color), as a function of time in the simulation, the magnetic field component along the radial direction (away from the Earth), B_r, along the magenta cut following the magnetopause signature shown in Figure 5a. More precisely, the values of B_r are taken along the intersection of the lines of sight forming this cut with the $Y = 0$ plane (noon–midnight meridional plane), and they approximately correspond to the magnetic

field component normal to the magnetopause surface. One can see that, at a given value of θ_{ESL} along the intersected cut, B_r exhibits pseudo-oscillations with amplitudes up to ±10 nT. These correspond to bipolar signatures as FTEs transit across the location. In the northern hemisphere, when the leading edge of a FTE approaches a given location at the dayside magnetopause, B_r is increased (red values in the plot), and as the trailing edge of the FTE passes the location, B_r shows a negative deflection (blue values). Due to the geometry, the situation is opposite in the southern hemisphere. Hence, we can see how FTEs tend to form within a few degrees from the subsolar point at the dayside magnetopause, and how they propagate toward one of the polar cusps in ~150 s. It is noteworthy that the propagation time of the identified FTEs is shorter than the image acquisition time which is retained in this study. However, one may want to determine whether FTEs can still create a signature in soft X-ray images integrated over 300 s.

In Figure 8b, we show the time-averaged value of the proton number density, $\langle n_p \rangle_{300s}$, along the intersection of the cut with the $Y = 0$ plane (i.e., at the locations where B_r is monitored). The time averaging is done over 300 s intervals corresponding to the integration time of the three images shown in Figure 4. It can be seen that (i) the time-averaged density along the magnetopause exhibits some variations as a function of θ_{ESL}, and (ii) these variations change from one 300 s interval to another. The largest differences occur at θ_{ESL} values comprised between 0° and −20° during the third time interval (1100–1400 s). During this time interval, three bipolar signatures can be identified in Figure 8a at those θ_{ESL} values. We can see in Movie S3 that these FTEs are indeed associated with higher-than-background proton number densities.

Grandin M et al.: Vlasiator simulation of solar wind charge exchange soft X-ray emissions
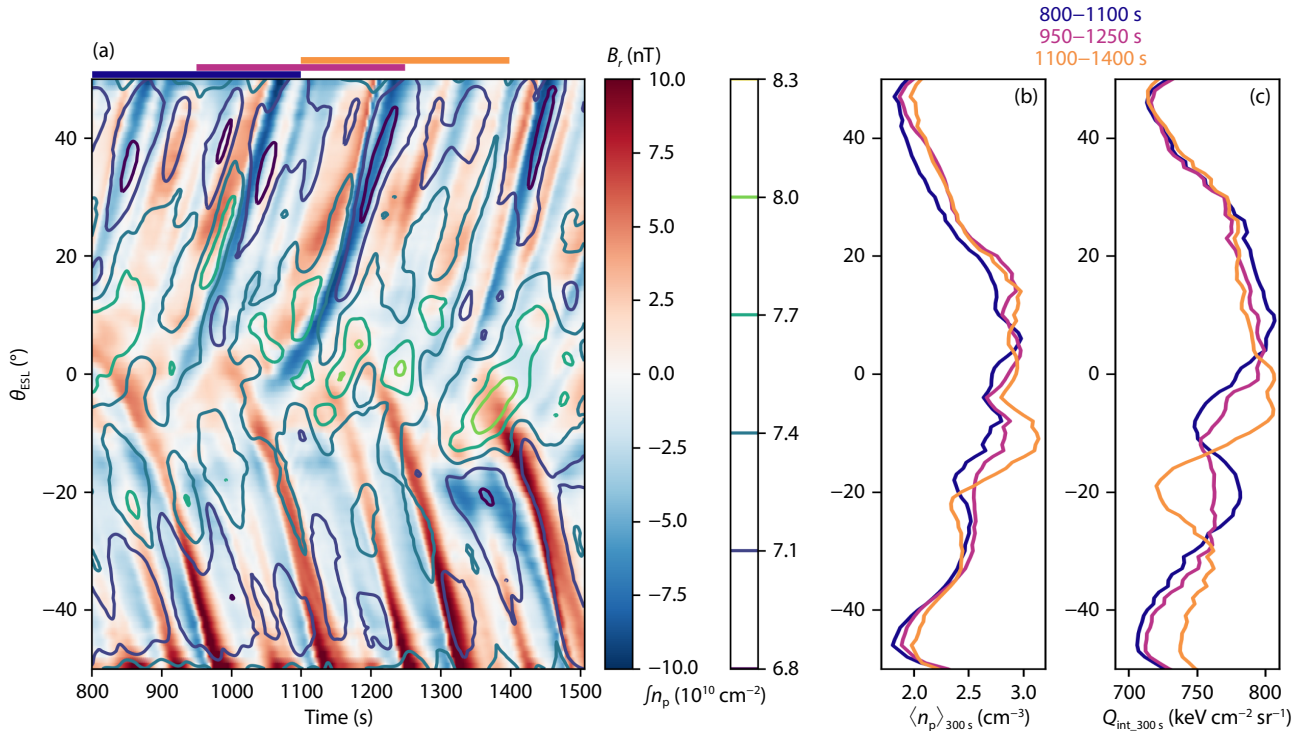
Figure 8. (a) Background color: Time evolution of the radial (i.e., nearly normal to the magnetopause) component of the magnetic field along the intersection of the magenta cut following the magnetopause signature in Figure 5a with the $Y = 0$ plane. FTEs generated near the subsolar point create a bipolar signature moving toward higher magnetopause angles as a function of time, with opposite polarity in opposite hemispheres. Isocontours: Time evolution of the line-of-sight-integrated proton number density along the magenta cut in Figure 5a. (b) Proton number density along the intersection of the cut with the $Y = 0$ plane, averaged over 300 s for the three studied time intervals (starting at $t = 800$ s, $t = 950$ s and $t=1100$ s). (c) Value of the 300 s-integrated soft X-ray emission along the cut in the corresponding three images shown in Figure 4 (same data as Figure 5f). The colored horizontal lines above panel (a) indicate the three studied time intervals.

Figure 8c reproduces the corresponding values of Q_{int_300s} during the three time intervals along the cut in the soft X-ray images (same data as in Figure 5f). While the match between the spatial and temporal variations in $\langle n_p \rangle_{300s}$ and Q_{int_300s} is not perfect, the corresponding curves do nonetheless exhibit striking resemblance. This suggests that the presence of FTEs at the dayside magnetopause during the image acquisition time can affect the average proton density along corresponding lines of sight and induce a signature in soft X-ray emission values. The imperfect match can be expected given that Q_{int_300s} values result from a line-of-sight integration, whereas the $\langle n_p \rangle_{300s}$ values are taken locally in the $Y = 0$ plane. We note, however, that the FTEs in this Vlasiator run can extend several Earth radii along the Y direction (see Figure S1 in the Supplementary Material). Hence, in this imaging geometry, increased soft X-ray emissivity can take place over a significant portion of the line of sight intersecting an FTE.

To investigate this further, overlaid with the B_r data in Figure 8a are isocontours of the proton number density integrated along the lines of sight forming the magenta cut in Figure 5a. As for the Q_{int_300s} shown in Figure 8c, this line-of-sight-integrated density likely contains effects of variations occurring outside of the $Y = 0$ plane; however, one can see a tendency for density enhancements to follow the pattern formed by the bipolar signatures associated with FTEs in the $Y = 0$ plane. This suggests that the proton density enhancements occurring in the core of the simulated FTEs can

produce soft X-ray signatures even in line-of-sight- and time-integrated images. It is worth mentioning that, in observations, FTEs often exhibit a density decrease in their core (Akhavan-Tafti et al., 2018). Yet, some observed FTEs do show a proton density increase and might therefore produce signatures in soft X-ray images similar to those described here (see Section 5)

4.2 Mirror-Mode Waves in the Magnetosheath

In Movie S3, one can identify wave-like structures in the magnetosheath consisting of patches of increased proton number density appearing in the central part of the magnetosheath (Earthward from the bow shock) and slowly drifting toward the magnetopause. In 2D–3V Vlasiator simulations, mirror-mode waves have been identified in the magnetosheath (Hoilijoki et al., 2016; Dubart et al., 2020). In a nearly 3D–3V setup wherein a noon–midnight meridional-plane slice with a thickness of 7 R_E along the dawn–dusk dimension was simulated with Vlasiator, Pfau-Kempf et al. (2020) identified anticorrelated magnetic field and proton density fluctuations in the magnetosheath, attributed to mirror-mode waves. We will first check whether in this 3D–3V run those waves exhibit similar properties as mirror-mode waves, after which we will investigate to what extent they can create signatures in soft X-ray images.

Figure 9 presents the magnetic field magnitude (Figure 9a–b), proton number density (Figure 9c–d) and local soft X-ray emissivity

(Figure 9e–f) along the intersections of the black and grey cuts in Figure 5a with the $Y = 0$ plane. These data are shown at four time steps in the simulation: $t = 1000$, 1010, 1020, and 1030 s. Here, the horizontal axis corresponds to the X coordinate of the cut intersection points in the $Y = 0$ plane to give a better intuition of spatial scales.

At $X < 9\,R_E$, the magnetic field magnitude decreases steadily and the proton density is on the order of 0.5 cm^{-3}, which corresponds to magnetosphere field and plasma. As X increases, the magnetic field magnitude drops more drastically, whereas the proton density increases. This corresponds to the crossing of the magnetopause. Beyond the magnetopause, one can notice fluctuations in both $|B|$ and n_p, with sizes on the order of 1–2 R_E along the X coordinate. These fluctuations are more prominent in the northern (black) cut than in the southern (grey) cut, and there is a fairly clear anticorrelation in the variations of both parameters. Besides, we can see that the structures associated with these fluctuations appear to drift Earthward by about 1 R_E in 40 s, giving an estimated speed along the X direction of ~150 km s^{-1}. Comparing with Figure 2b, we can infer that the structures therefore approximately drift alongside the plasma. The anticorrelation between magnetic field and density variations and the fact that the waves are roughly static in the plasma frame strongly suggest that these waves are indeed mirror modes. The interhemispheric asymmetry mentioned above likely arises from the fact that small numerical

effects (e.g., rounding errors) lead to mirror-mode structures not being exactly symmetrical in both hemispheres at a given time in the simulation.

Given the significant propagation of the mirror-mode waves over the span of 40 s seen in Figure 9, one cannot expect that individual wave fronts will be visible in an image integrated over 300 s. However, like for FTEs, one can investigate whether mirror-mode wave activity in the magnetosheath can nevertheless produce a signature in soft X-ray images. Figure 10 presents this analysis along the same cuts as Figure 9, but this time for time-averaged parameters along the cut, again using the same three 300 s time intervals as previously. In all panels of this figure, the horizontal axis corresponds to the angular distance d to the origin of the azimuth–elevation frame used in soft X-ray images.

In Figures 10a–b, we show the time-averaged magnetic field magnitude along the cuts during the three intervals. While the magnetosphere and magnetopause values do not differ significantly during the three intervals, one can see that the magnetosheath fluctuations, associated with the mirror-mode waves identified previously, differ slightly from each other. The differences appear more clearly in the time-averaged proton density panels (Figures 10c–d), especially at $d \approx 21 - 26°$, and the resulting time-averaged local soft X-ray emission values ($\langle Q_{loc}\rangle_{300s}$, Figures 10e–f) in the $Y = 0$ plane are consistent with average density fluc-
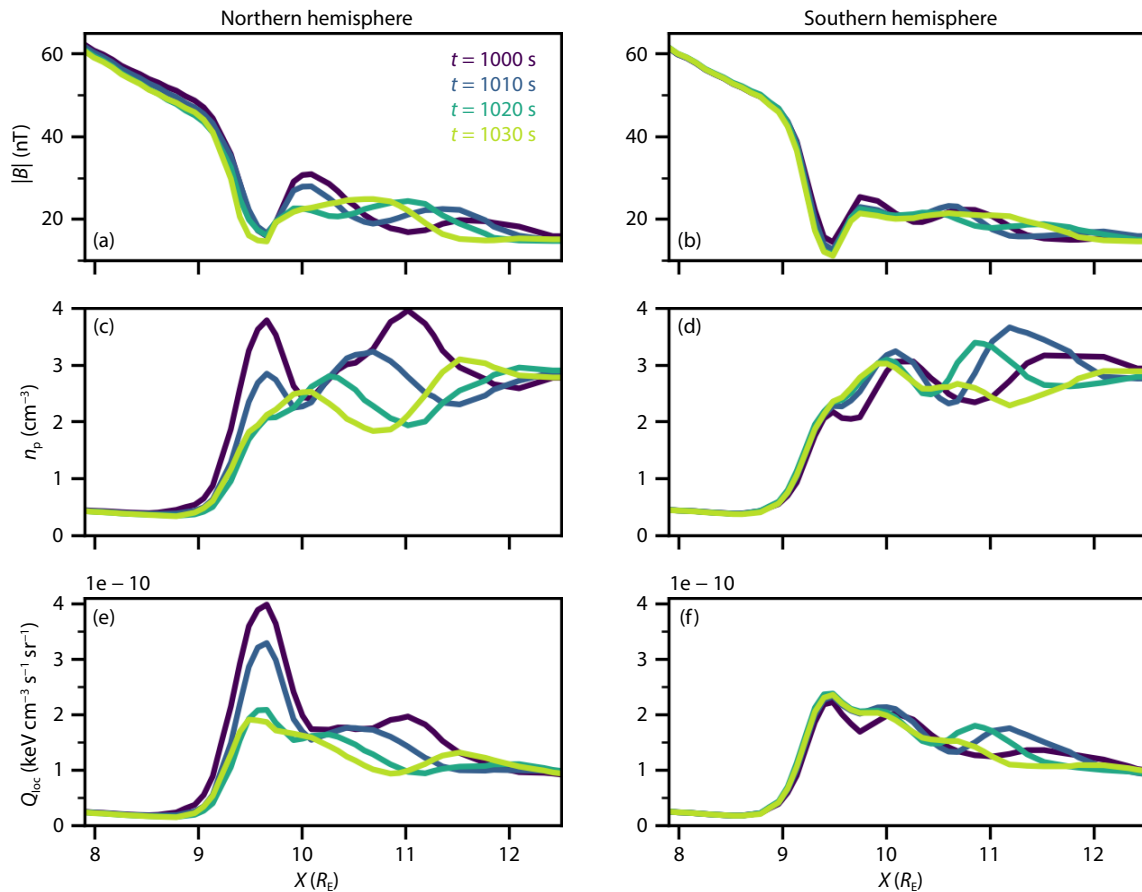

Figure 9. Investigation of the magnetosheath waves signatures along the black and grey cuts in Figure 5a. The shown variables are taken along the intersections of the cuts with the $Y = 0$ plane at four time steps in the simulation (i.e., these are instantaneous values). (a–b) Magnetic field magnitude. (c–d) Proton number density. (e–f) Local soft X-ray emissivity.
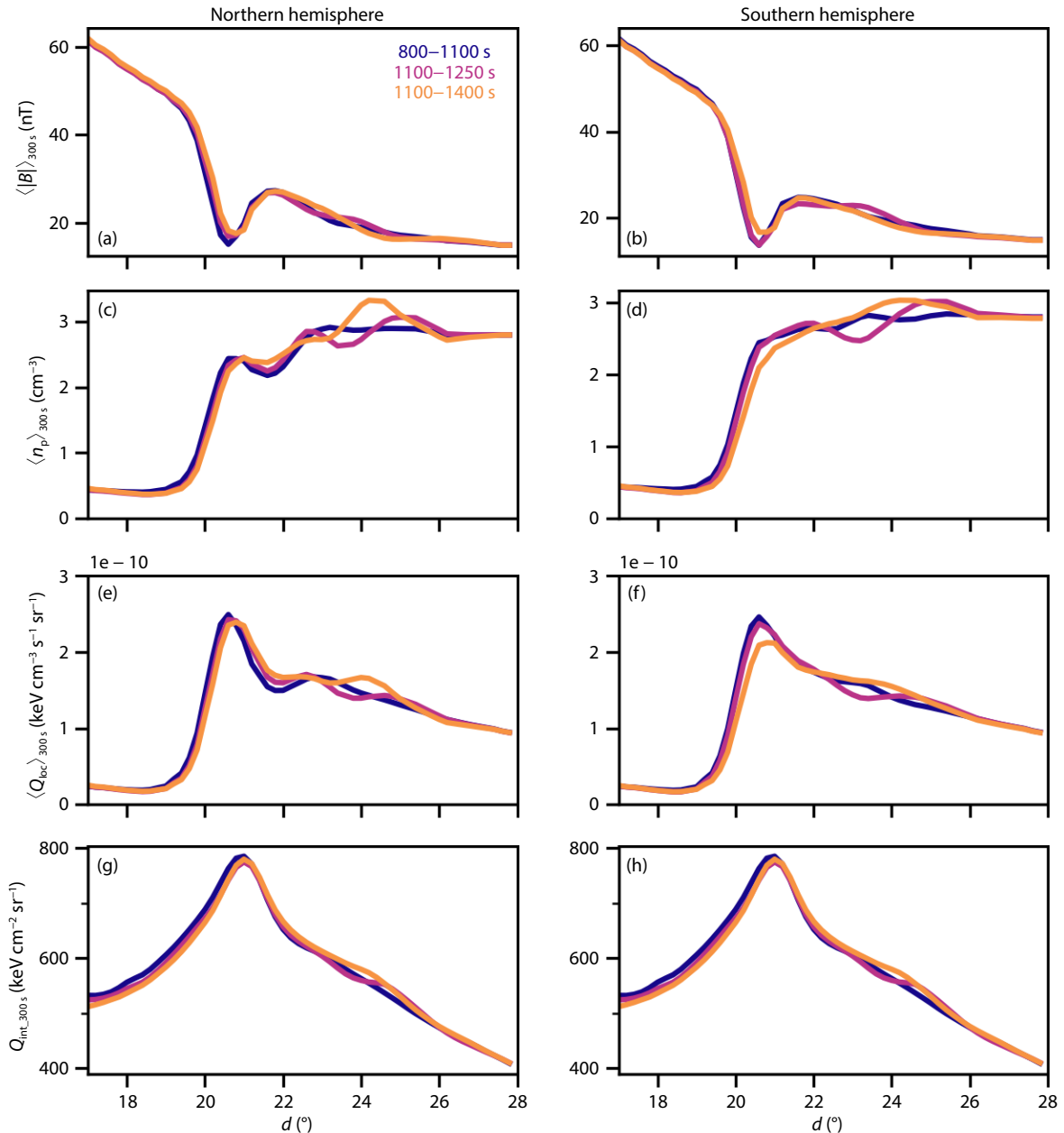
Grandin M et al.: Vlasiator simulation of solar wind charge exchange soft X-ray emissions

Figure 10. Time-averaged values of the magnetosheath parameters shown in Figure 9 over 300 s intervals starting at t = 800 s, t = 950 s, and t=1100 s. (a–b) Time-averaged magnetic field magnitude along the intersections of the black and grey cuts with the Y = 0 plane, respectively. (c–d) Same for the time-averaged proton number density. (e–f) Same for the time-averaged local soft X-ray emissivity. (g–h) Soft X-ray emission values along the black and grey cuts in the 300 s-integrated images shown in Figure 4. The last two panels show the same data as Figure 5b–c.

tuations. These asymmetries are however less prominent than those seen in Figure 9, because the 300 s averaging smooths them out. To assess the effect of these local time-averaged fluctuations in actual soft X-ray images, Figures 10g–h show the soft X-ray emissions integrated along the line of sight corresponding to the two cuts (same data as in Figure 5b–c, respectively). In these panels, we can see that the three lines corresponding to the three time intervals do not fully overlap within $d \approx 22{-}26°$.

5. Discussion

First of all, it is worth comparing the soft X-ray emissivity values obtained with the Vlasiator simulation to those reported in

modeling studies using different models. Sun TR et al. (2019) carried out a series of soft X-ray emission simulations using a MHD model, driven by various types of solar wind conditions. Our driving conditions correspond closest to their first case, with a solar wind density of 5 cm^{-3}, a solar wind speed of 400 km s^{-1}, and a purely southward IMF of 5 nT magnitude. They obtained a soft X-ray image from a virtual imaging satellite approximately positioned above the north pole (analogous to our Figure 3d), in which the magnetopause signature reached a value of 13 keV cm^{-2} s^{-1} sr^{-1}. In contrast, with our Vlasiator run, we get a value close to 3 keV cm^{-2} s^{-1} sr^{-1}, which is almost a factor of 5 lower. This is consistent with our solar wind density being 5 times lower than theirs, leading

to a magnetosheath density accordingly lower. Our values are also in fairly good agreement with those obtained by Connor et al. (2021) using a simulation from the OpenGGCM global MHD model and providing soft X-ray images seen from the dawnside (analogous to our Figure 2d).

While Vlasiator is too computationally expensive to be run over a long time interval, its unique advantage is that the hybrid-kinetic description of the space plasma enables the formation of transient features which cannot emerge in MHD simulations. We can therefore simulate the possible effect of such phenomena in soft X-ray images of the near-Earth space as will be obtained by SMILE and LEXI. Considering first the case of FTEs, if we focus on the largest peak-to-trough variation of Q_{int_300s} in Figure 8c, corresponding to the 1100–1400 s time interval and θ_{ESL} angles between −20° and 0°, we obtain $\Delta Q_{int\_300s} \approx 90$ keV cm^{-2} sr^{-1}, amounting to about 12% of the background value along the dayside magnetopause. The corresponding spatial variations in proton density in the $Y = 0$ plane amount to 0.81 cm^{-3}, on the order of 30% of the background value. This can provide quantitative elements to assess whether a soft X-ray imager might be able to detect signatures associated with FTEs, depending on the specifications of the soft X-ray sensor.

FTEs have been found to form at the dayside magnetopause quasiperiodically appearing approximately once every 8 minutes (Rijnbeek et al., 1984) preferably forming during southward IMF conditions (e.g., Berchem and Russell, 1984). A statistical study of 55 FTEs using MMS observations found an average size of a subsolar FTE to be 1700 ± 400 km (Akhavan-Tafti et al., 2018), which is 3 to 7 times smaller than the FTEs observed at the higher latitudes (Y. L. Wang C et al., 2005; Fermo et al., 2011; Akhavan-Tafti et al., 2018). However, the scale sizes of the observed FTEs vary from ionscale flux ropes (e.g., Eastwood et al., 2016; Dong XC et al., 2017) to FTEs with a diameter up to 1–2 R_E (Rijnbeek et al., 1984; Hasegawa et al., 2006; Fear et al., 2007), while their axial length can be much longer (e.g., Fear et al., 2008).

A typical FTE has an internal structure with twisted field lines and axial magnetic field leading to an increase in total magnetic field magnitude and a decrease in the density in the core of the FTE (e.g., Akhavan-Tafti et al., 2018; Zhang H et al., 2010). However, "crater" FTEs with a decrease in total magnetic field with a higher density in the middle have been observed (Zhang H et al., 2010). A statistical study of 18 typical and 14 crater FTEs comparing FTE densities (n_{FTE}) and magnetic field strength (B_{FTE}) to the magnetosheath density (n_{MS}) and magnetic field (B_{MS}) showed that 75% of typical FTEs have the density ratio $n_{FTE}/n_{MS} < 0.5$ and 80% of the FTEs have $B_{FTE} > B_{MS}$, while 90% of the crater FTEs had $n_{FTE}/n_{MS} > 0.5$ (and approximately 50% $n_{FTE} > n_{MS}$) and approximately 95% had smaller magnetic field magnitude than the surrounding magnetosheath (Zhang et al., 2010). Recent particlein-cell (PIC) simulations have revealed the important role of a guide field in FTEs. A local PIC study showed that, if the guide field is strong, FTEs exhibit low density in their core, whereas a weak guide field results in enhanced proton density within the FTE (Lu S et al., 2020). These results have been confirmed in a global PIC study, wherein purely southward IMF ($B_y = 0$, no guide field) leads

to density increase in FTEs whereas driving conditions with a nonzero IMF B_y (i.e. with a guide field) lead to FTEs exhibiting a density decrease in their core (Guo J et al., 2021). In this Vlasiator simulation, the IMF is purely southward, and the identified FTEs have a higher-than-background proton density in their core. This result is consistent with those from Guo J et al. (2021). We can therefore speculate that soft X-ray images might be able to capture signatures of FTEs when their guide field is weak ($B_y \approx 0$), even more so if their peak-to-trough density variation is similar to or greater than that of FTEs identified in this simulation. However, we can anticipate that FTEs forming in presence of a strong guide field ($B_y \neq 0$) would not produce bright signatures in soft X-ray images.

It is clear from the presented results that FTEs forming in this Vlasiator run move across a 300 s integrated soft X-ray image too fast for them to be individually visible in the image. Rather, the local soft X-ray emission enhancements in some parts of the magnetopause signature are likely due to the cumulative effect of several FTEs, especially if these tend to remain longer at a given latitude. Hoilijoki et al. (2019) showed that the speed at which FTEs propagate toward higher latitudes along the magnetopause depends on the driving conditions. We can therefore speculate that, in some cases where the FTE motion is slower than in this simulation, their signatures in soft X-ray images might be more prominent than in the results obtained here.

Regarding mirror-mode waves in the magnetosheath, we can estimate the effect of the largest density enhancement visible in Figure 10c. Considering the difference between the $\langle n_p \rangle_{300s}$ values during the first and third time intervals at $d = 24°$, we find that it consists of a local density enhancement by 0.4 cm^{-3} (~14%) in the $Y = 0$ plane associated with mirror-mode waves structures. The corresponding difference in time-integrated soft X-ray emissions amounts to about 20 keV cm^{-2} sr^{-1} (~4%).

Mirror-mode structures are large-scale compressional waves that are non-propagating in the plasma frame. They are often observed in the Earth's magnetosheath especially behind the quasi-perpendicular bow shock. They may appear as quasi-sinusoidal oscillations in the magnetic field but mirror-mode structures are often observed as peaks in the mirror-unstable plasma and dips in mirror-stable conditions near the magnetopause (Soucek et al., 2008). The depth of the mirror structures has been found to increase with the decreasing distance to the magnetopause (Soucek et al., 2008). The analysis of 2 months of Cluster data by Soucek et al. (2008) showed that the average period of the mirrormode waves was approximately 12 s (with 98% of the observed structures being between 4 to 24 s). A statistical study by Lucek et al. (2001) showed that the scale sizes of the mirror structures can vary from less than 600 km along the local magnetopause normal, 750–1000 km along the maximum variance direction to 1500–3000 km along the flow direction. The amplitude of the magnetic field variations associated with mirror-mode waves is typically on the order of several 10% of the background field, and the associated proton density variations can lead to up to multi-fold local enhancements (e.g., Chandler et al., 2021).

The differences in Q_{int_300s} values obtained above are estimates

under the driving conditions and the setup used in the Vlasiator run on which this study is based. These choices and constraints have several consequences on the properties of the mirror-mode waves. First of all, in our simulation, the spatial resolution in the magnetosheath (2000 km) likely leads to mirror-mode structures being larger than in reality. Therefore, one may speculate that SMILE and LEXI observations of mirror-mode structures would likely be smaller and might hence be blurred out more easily than in this simulation.

Besides, Dubart et al. (2020) showed that, when the spatial resolution of a Vlasiator simulation is too coarse, the unstable proton distributions in the magnetosheath entirely pump their free energy into the growth of mirror-mode structures, instead of transferring part of it to electromagnetic ion cyclotron waves, which require a finer spatial resolution to emerge. It is worth noting, however, that the solar wind driving conditions used in the run are not the most typical ones. Indeed, the solar wind density is notably lower than average, whereas the solar wind velocity and temperatures are higher than average. This suggests that, under solar wind conditions closer to average values than in this Vlasiator run, such as those from Sun TR et al. (2019) discussed above, larger signal than what we obtained can be expected. This, combined with the fact that density fluctuations associated with mirror-mode waves can be greater than in our simulation (factor of 3 in the event analyzed by Chandler et al. (2021)), suggests that the constraints on FTEs and mirror-mode waves for them to produce signatures in the soft X-ray observations of LEXI and SMILE might actually be less strict than suggested by our results. Additional simulations with a finer spatial resolution and different solar wind driving are needed to test this hypothesis.

Another point worth discussing is that the Vlasiator run duration analyzed for this study consists of a 700 s time interval only. In reality, both LEXI and SMILE SXI instruments will observe processes over significantly longer time scales, which could open more possibilities for the data analysis. For instance, calculating the discrepancy between two time-integrated images separated by a few minutes could enhance contrast in regions where the plasma conditions have changed during that time frame. While this would likely still not enable the detection and monitoring of individual structures given the required image acquisition time, this could provide additional approaches to indirectly identify such processes in near-Earth space, as well as context for in-situ observations.

Finally, one should point out the fact that, in this Vlasiator run, the driving conditions are steady. As a consequence, one may expect that the large-scale features such as the boundary locations (bow shock, magnetopause, polar cusps) do not change much during the studied time interval. Nevertheless, Figures 5d–e indicate that the cusp signatures slightly move toward higher latitudes with time, possibly in response to processes occurring on the nightside in this simulation (not shown). This suggests that the analysis of successive soft X-ray images might enable the tracking of boundary motions. To confirm this, it would prove interesting to monitor the motion of these boundaries in a Vlasiator run in which solar wind conditions are varying. This is a future avenue for an upcoming study which could be made possible once a Vlasiator run with time-varying driving conditions is available.

6. Conclusions

In this paper, we presented the first estimates of SWCX soft X-ray emission imaging of the dayside near-Earth space based on a hybrid-Vlasov simulation. We used ~700 s of a Vlasiator run driven by constant solar wind of low density and high velocity and with purely southward IMF with $B_z = -5$ nT. From the Vlasiator simulation outputs, we calculated at every second the local soft X-ray emissivity based on the plasma parameters and produced line-of-sight-integrated instantaneous soft X-ray images as would be obtained from a virtual imaging spacecraft placed at a distance of $30\,R_E$ from the Earth's center, providing the polar and side views of the Earth's magnetosphere similar to the SMILE and LEXI views, respectively. We then integrated those instantaneous images over 300 s intervals to reproduce anticipated observational requirements for the SMILE and LEXI SXI instruments. The main results of this study are as follows:

(1) The most prominent features in soft X-ray images obtained from above the pole or on the dawnside consist of the magnetopause and polar cusps (the latter only when observing from the dawnside). The soft X-ray emissivity values obtained with Vlasiator are consistent with earlier MHD results, taking into account differences in the solar wind driving conditions.

(2) Despite the 300 s integration time, the obtained soft X-ray images exhibit smaller-scale features such as the brightening of localized areas at the dayside magnetopause and wave-like patterns in the magnetosheath signature. These features are created by transient phenomena, namely FTEs and mirror-mode waves, respectively.

(3) Based on the simulated soft X-ray images, one can anticipate that FTE signatures could amount to 12% of the background signal if FTEs occurring during the 300 s interval cumulatively lead to local proton density enhancements by about 30%. This result holds for FTEs whose guide field is weak (when IMF $B_y \approx 0$), which exhibit enhanced proton density in their core (Lu S et al., 2020; Guo J et al., 2021). One can expect that FTEs with a strong guide field, which contain low-density plasma, would not produce bright signatures in soft X-ray images.

(4) Correspondingly, soft X-ray images of SMILE and LEXI might reveal the presence of mirror-mode waves, as in the simulation the associated density structures in the magnetosheath cumulatively led to an enhancement by 14% in the proton density, locally, and produced an increase in soft X-ray emission signal by 4%. Depending on the scale size, propagation speed and amplitude of the variations in the proton density, mirror-mode structures may lead to more pronounced or on the contrary more blurred out signatures in soft X-ray images.

(5) The above values are likely conservative estimates, given that the solar wind conditions in this Vlasiator run are representative of solar wind high-speed streams rather than the more common average solar wind driving which typically has larger proton number density.

The results of this study contribute to the SMILE Modeling Working

Group objectives by comparing simulation results using a hybrid-Vlasov code with other works based on MHD. Moreover, the hybrid-kinetic description of the space plasma provides a unique opportunity to anticipate under what conditions transient processes in the dayside near-Earth space might be observed by soft X-ray imagers on SMILE and LEXI. Future plans could include the monitoring of the motion of the large-scale space plasma boundaries (magnetopause, polar cusps, bow shock) in a different run with time-varying upstream conditions (for instance a dynamic pressure increase or a rotation of the IMF).

The authors declare that they have no conflict of interest.

The Vlasiator simulation data used in the study amount to 18 TB of disk space; access to the raw simulation data can be granted by following the Vlasiator data access policy (see https://www2.helsinki.fi/en/researchgroups/vlasiator/rules-of-the-road). The Vlasiator code is preserved at https://zenodo.org/record/3640593 (PfauKempf et al., 2022), available in open access. It is developed openly at https://github.com/fmihpc/vlasiator.

References

Akhavan-Tafti, M., Slavin, J. A., Le, G., Eastwood, J. P., Strangeway, R. J., Russell, C. T., Nakamura, R., Baumjohann, W., Torbert, R. B., … Burch, J. L. (2018). MMS examination of FTEs at the Earth's subsolar magnetopause. *J. Geophys. Res.: Space Phys.*, *123*(2), 1224–1241. https://doi.org/10.1002/2017JA024681

Ala-Lahti, M., Pulkkinen, T. I., Pfau-Kempf, Y., Grandin, M., and Palmroth, M. (2022). Energy flux through the magnetopause during flux transfer events in hybrid-Vlasov 2D simulations. *Geophys. Res. Lett.*, *49*(19), e2022GL100079. https://doi.org/10.1029/2022GL100079

Atz, E. A., Walsh, B. M., Broll, J. M., and Zou, Y. (2022). The spatial extent of magnetopause magnetic reconnection from in situ THEMIS measurements. *J. Geophys. Res.: Space Phys.*, *127*(12), e2022JA030894. https://doi.org/10.1029/2022JA030894

Battarbee, M., Blanco-Cano, X., Turc, L., Kajdič, P., Johlander, A., Tarvus, V., Fuselier, S., Trattner, K., Alho, M., … Palmroth, M. (2020a). Helium in the Earth's foreshock: a global Vlasiator survey. *Ann. Geophys.*, *38*(5), 1081–1099. https://doi.org/10.5194/angeo-38-1081-2020

Battarbee, M., Ganse, U., Pfau-Kempf, Y., Turc, L., Brito, T., Grandin, M., Koskela, T., and Palmroth, M. (2020b). Non-locality of Earth's quasi-parallel bow shock: injection of thermal protons in a hybrid-Vlasov simulation. *Ann. Geophys.*, *38*(3), 625–643. https://doi.org/10.5194/angeo-38-625-2020

Berchem, J., and Russell, C. T. (1984). Flux transfer events on the magnetopause: spatial distribution and controlling factors. *J. Geophys. Res.: Space Phys.*, *89*(A8), 6689–6703. https://doi.org/10.1029/JA089iA08p06689

Branduardi-Raymont, G., Wang, C., Escoubet, C. P., Adamovic, M., Agnolon, D., Berthomier, M., Carter, J. A., Chen, W., Colangeli, L., … Zhu, Z. (2018). *SMILE Definition Study Report* (Red Book). European Space Agency, *ESA/SCI*, 1. https://doi.org/10.5270/esa.smile.definition_study_report-2018-12

Carter, J. A., Sembay, S., and Read, A. M. (2010). A high charge state coronal mass ejection seen through solar wind charge exchange emission as detected by *XMM-Newton*. *Mon. Not. Roy. Astron. Soc.*, *402*(2), 867–878. https://doi.org/10.1111/j.1365-2966.2009.15985.x

Carter, J. A., Sembay, S., and Read, A. M. (2011). Identifying XMM-*Newton* observations affected by solar wind charge exchange-Part II. *Astron. Astrophys.*, *527*, A115. https://doi.org/10.1051/0004-6361/201015817

Chandler, M. O., Schwartz, S. J., Avanov, L. A., Coffey, V. N., Giles, B. L., Moore, T. E., Pollock, C. J., Burch, J. L., Russell, C. T., and Torbert, R. B. (2021). Observations of mirror mode structures in the dawn-side magnetosphere. *J. Geophys. Res.: Space Phys.*, *126*(2), e2020JA028649. https://doi.org/10.1029/2020JA028649

Collier, M. R., and Connor, H. K. (2018). Magnetopause surface reconstruction from tangent vector observations. *J. Geophys. Res.: Space Phys.*, *123*(12), 10189–10199. https://doi.org/10.1029/2018JA025763

Connor, H. K., and Carter, J. A. (2019). Exospheric neutral hydrogen density at the nominal 10 R_E subsolar point deduced from XMM-Newton X-ray observations. *J. Geophys. Res.: Space Phys.*, *124*(3), 1612–1624. https://doi.org/10.1029/2018JA026187

Connor, H. K., Sibeck, D. G., Collier, M. R., Baliukin, I. I., Branduardi-Raymont, G., Brandt, P. C., Buzulukova, N. Y., Collado-Vega, Y. M., Escoubet, C. P., … Zoennchen, J. H. (2021). Soft X-ray and ENA imaging of the Earth's dayside magnetosphere. *J. Geophys. Res.: Space Phys.*, *126*(3), e2020JA028816. https://doi.org/10.1029/2020JA028816

Cox, D. P. (1998). Modeling the local bubble. In D. Breitschwerdt, et al. (Eds.), *The Local Bubble and Beyond Lyman-Spitzer-Colloquium* (pp. 121-131). Berlin, Heidelberg: Springer.

Cravens, T. E., Robertson, I. P., and Snowden, S. L. (2001). Temporal variations of geocoronal and heliospheric X-ray emission associated with the solar wind interaction with neutrals. *J. Geophys. Res.: Space Phys.*, *106*(A11), 24883–24892. https://doi.org/10.1029/2000JA000461

Dong, X. C., Dunlop, M. W., Trattner, K. J., Phan, T. D., Fu, H. S., Cao, J. B., Russell, C. T., Giles, B. L., Torbert, R. B., … Burch, J. L. (2017). Structure and evolution of flux transfer events near dayside magnetic reconnection dissipation region: MMS observations. *Geophys. Res. Lett.*, *44*(12), 5951–5959. https://doi.org/10.1002/2017GL073411

Dubart, M., Ganse, U., Osmane, A., Johlander, A., Battarbee, M., Grandin, M., Pfau-Kempf, Y., Turc, L., and Palmroth, M. (2020). Resolution dependence of magnetosheath waves in global hybrid-Vlasov simulations. *Ann. Geophys.*, *38*(6), 1283–1298. https://doi.org/10.5194/angeo-38-1283-2020

Eastwood, J. P., Phan, T. D., Cassak, P. A., Gershman, D. J., Haggerty, C., Malakit, K., Shay, M. A., Mistry, R., Øieroset, M., … Wang, S. (2016). Ion-scale secondary flux ropes generated by magnetopause reconnection as resolved by MMS. *Geophys. Res. Lett.*, *43*(10), 4716–4724. https://doi.org/10.1002/2016GL068747

Fear, R. C., Milan, S. E., Fazakerley, A. N., Owen, C. J., Asikainen, T., Taylor, M. G. G. T., Lucek, E. A., Rème, H., Dandouras, I., and Daly, P. W. (2007). Motion of flux transfer events: a test of the Cooling model. *Ann. Geophys.*, *25*(7), 1669–1690. https://doi.org/10.5194/angeo-25-1669-2007

Fear, R. C., Milan, S. E., Fazakerley, A. N., Lucek, E. A., Cowley, S. W. H., and Dandouras, I. (2008). The azimuthal extent of three flux transfer events. *Ann. Geophys.*, *26*(8), 2353–2369. https://doi.org/10.5194/angeo-26-2353-2008

Fermo, R. L., Drake, J. F., Swisdak, M., and Hwang, K. J. (2011). Comparison of a statistical model for magnetic islands in large current layers with Hall MHD simulations and Cluster FTE observations. *J. Geophys. Res.: Space Phys.*, *116*(A9), A09226. https://doi.org/10.1029/2010JA016271

Grandin, M., Battarbee, M., Osmane, A., Ganse, U., Pfau-Kempf, Y., Turc, L., Brito,

T., Koskela, T., Dubart, M., and Palmroth, M. (2019). Hybrid-Vlasov modelling of nightside auroral proton precipitation during southward interplanetary magnetic field conditions. *Ann. Geophys.*, *37*(5), 791–806. https://doi.org/10.5194/angeo-37-791-2019

Grandin, M., Turc, L., Battarbee, M., Ganse, U., Johlander, A., Pfau-Kempf, Y., Dubart, M., and Palmroth, M. (2020). Hybrid-Vlasov simulation of auroral proton precipitation in the cusps: comparison of northward and southward interplanetary magnetic field driving. *J. Space Wea. Space Climate*, *10*, 51. https://doi.org/10.1051/swsc/2020053

Guo, J., Lu, S., Lu, Q. M., Lin, Y., Wang, X. Y., Huang, K., Wang, R. S., and Wang, S. (2021). Structure and coalescence of magnetopause flux ropes and their dependence on IMF clock angle: three-dimensional global hybrid simulations. *J. Geophys. Res.: Space Phys.*, *126*(2), e2020JA028670. https://doi.org/10.1029/2020JA028670

Hasegawa, A. (1969). Drift mirror instability in the magnetosphere. *Phys. Fluids*, *12*(12), 2642–2650. https://doi.org/10.1063/1.1692407

Hasegawa, H., Sonnerup, B. U. Ö., Owen, C. J., Klecker, B., Paschmann, G., Balogh, A., and Rème, H. (2006). The structure of flux transfer events recovered from cluster data. *Ann. Geophys.*, *24*(2), 603–618. https://doi.org/10.5194/angeo-24-603-2006

Hoilijoki, S., Palmroth, M., Walsh, B. M., Pfau-Kempf, Y., von Alfthan, S., Ganse, U., Hannuksela, O., and Vainio, R. (2016). Mirror modes in the Earth's magnetosheath: results from a global hybrid-Vlasov simulation. *J. Geophys. Res.: Space Phys.*, *121*(5), 4191–4204. https://doi.org/10.1002/2015JA022026

Hoilijoki, S., Ganse, U., Pfau-Kempf, Y., Cassak, P. A., Walsh, B. M., Hietala, H., von Alfthan, S., and Palmroth, M. (2017). Reconnection rates and X line motion at the magnetopause: global 2D-3V hybrid-Vlasov simulation results. *J. Geophys. Res.: Space Phys.*, *122*(3), 2877–2888. https://doi.org/10.1002/2016JA023709

Hoilijoki, S., Ganse, U., Sibeck, D. G., Cassak, P. A., Turc, L., Battarbee, M., Fear, R. C., Blanco-Cano, X., Dimmock, A. P., … Palmroth, M. (2019). Properties of magnetic reconnection and FTEs on the dayside magnetopause with and without positive IMF B_x component during southward IMF. *J. Geophys. Res.: Space Phys.*, *124*(6), 4037–4048. https://doi.org/10.1029/2019JA026821

Jung, J., Connor, H. K., Carter, J. A., Koutroumpa, D., Pagani, C., and Kuntz, K. D. (2022). Solar minimum exospheric neutral density near the subsolar magnetopause estimated from the XMM soft X-ray observations on 12 November 2008. *J. Geophys. Res.: Space Phys.*, *127*(3), e2021JA029676. https://doi.org/10.1029/2021JA029676

Juusola, L., Pfau-Kempf, Y., Ganse, U., Battarbee, M., Brito, T., Grandin, M., Turc, L., and Palmroth, M. (2018). A possible source mechanism for magnetotail current sheet flapping. *Ann. Geophys.*, *36*(4), 1027–1035. https://doi.org/10.5194/angeo-36-1027-2018

Londrillo, P., and Del Zanna, L. (2004). On the divergence-free condition in Godunov-type schemes for ideal magnetohydrodynamics: the upwind constrained transport method. *J. Comput. Phys.*, *195*(1), 17–48. https://doi.org/10.1016/j.jcp.2003.09.016

Lu, S., Angelopoulos, V., Artemyev, A. V., Pritchett, P. L., Sun, W. J., and Slavin, J. A. (2020). Particle-in-cell simulations of secondary magnetic islands: ion-scale flux ropes and plasmoids. *Astrophys. J.*, *900*(2), 145. https://doi.org/10.3847/1538-4357/abaa44

Lucek, E. A., Dunlop, M. W., Horbury, T. S., Balogh, A., Brown, P., Cargill, P., Carr, C., Fornaçon, K. H., Georgescu, E., and Oddy, T. (2001). Cluster magnetic field observations in the magnetosheath: four-point measurements of mirror structures. *Ann. Geophys.*, *19*(10-12), 1421–1428. https://doi.org/10.5194/angeo-19-1421-2001

Palmroth, M., Ganse, U., Pfau-Kempf, Y., Battarbee, M., Turc, L., Brito, T., Grandin, M., Hoilijoki, S., Sandroos, A., and von Alfthan, S. (2018). Vlasov methods in space physics and astrophysics. *Living Rev. Comput. Astrophys.*, *4*(1), 1. https://doi.org/10.1007/s41115-018-0003-2

Papadakis, K., Pfau-Kempf, Y., Ganse, U., Battarbee, M., Alho, M., Grandin, M., Dubart, M., Turc, L., Zhou, H. Y., … Palmroth, M. (2022). Spatial filtering in a 6D hybrid-Vlasov scheme to alleviate adaptive mesh refinement artifacts: a case study with Vlasiator (versions 5.0, 5.1, and 5.2.1). *Geosci. Model Dev.*,

15(20), 7903–7912. https://doi.org/10.5194/gmd-15-7903-2022

Pfau-Kempf, Y., Palmroth, M., Johlander, A., Turc, L., Alho, M., Battarbee, M., Dubart, M., Grandin, M., and Ganse, U. (2020). Hybrid-Vlasov modeling of three-dimensional dayside magnetopause reconnection. *Phys. Plasmas*, *27*(9), 092903. https://doi.org/10.1063/5.0020685

Pfau-Kempf, Y., von Alfthan, S., Sandroos, A., Ganse, U., Koskela, T., Battarbee, M., and Alho, M. (2022). fmihpc/vlasiator: Vlasiator [dataset]. Zenodo. Retrieved from https://doi.org/10.5281/ZENODO.3640593

Rijnbeek, R. P., Cowley, S. W. H., Southwood, D. J., and Russell, C. T. (1984). A survey of dayside flux transfer events observed by ISEE 1 and 2 magnetometers. *J. Geophys. Res.: Space Phys.*, *89*(A2), 786–800. https://doi.org/10.1029/JA089iA02p00786

Robertson, I. P., and Cravens, T. E. (2003a). Spatial maps of heliospheric and geocoronal X-ray intensities due to the charge exchange of the solar wind with neutrals. *J. Geophys. Res.: Space Phys.*, *108*(A10), 8031. https://doi.org/10.1029/2003JA009873

Robertson, I. P., and Cravens, T. E. (2003b). X-ray emission from the terrestrial magnetosheath. *Geophys. Res. Lett.*, *30*(8), 1439. https://doi.org/10.1029/2002GL016740

Robertson, I. P., Collier, M. R., Cravens, T. E., and Fok, M. C. (2006). X-ray emission from the terrestrial magnetosheath including the cusps. *J. Geophys. Res.: Space Phys.*, *111*(A12), A12105. https://doi.org/10.1029/2006JA011672

Russell, C. T., and Elphic, R. C. (1978). Initial ISEE magnetometer results: magnetopause observations. *Space Sci. Rev.*, *22*(6), 681–715. https://doi.org/10.1007/BF00212619

Sibeck, D. G., Allen, R., Aryan, H., Bodewits, D., Brandt, P., Branduardi-Raymont, G., Brown, G., Carter, J. A., Collado-Vega, Y. M., … Wing, S. (2018). Imaging plasma density structures in the soft X-rays generated by solar wind charge exchange with neutrals. *Space Sci. Rev.*, *214*(4), 79. https://doi.org/10.1007/s11214-018-0504-7

Snowden, S. L., Freyberg, M. J., Plucinsky, P. P., Schmitt, J. H. M. M., Truemper, J., Voges, W., Edgar, R. J., McCammon, D., and Sanders, W. T. (1995). First maps of the soft X-ray diffuse background from the ROSAT XRT/PSPC all-sky survey. *Astrophys. J.*, *454*, 643. https://doi.org/10.1086/176517

Snowden, S. L., Collier, M. R., and Kuntz, K. D. (2004). *XMM-Newton* observation of solar wind charge exchange emission. *Astrophys. J.*, *610*(2), 1182–1190. https://doi.org/10.1086/421841

Soucek, J., Lucek, E., and Dandouras, I. (2008). Properties of magnetosheath mirror modes observed by cluster and their response to changes in plasma parameters. *J. Geophys. Res.: Space Phys.*, *113*(A4), A04203. https://doi.org/10.1029/2007JA012649

Sun, T. R., Wang, C., Sembay, S. F., Lopez, R. E., Escoubet, C. P., Branduardi-Raymont, G., Zheng, J. H., Yu, X. Z., Guo, X. C., … Guo, Y. H. (2019). Soft X-ray imaging of the magnetosheath and cusps under different solar wind conditions: MHD simulations. *J. Geophys. Res.: Space Phys.*, *124*(4), 2435–2450. https://doi.org/10.1029/2018JA026093

Sun, T. R., Wang, C., Connor, H. K., Jorgensen, A. M., and Sembay, S. (2020). Deriving the magnetopause position from the soft X-ray image by using the tangent fitting approach. *J. Geophys. Res.: Space Phys.*, *125*(9), e2020JA028169. https://doi.org/10.1029/2020JA028169

Tarvus, V., Turc, L., Battarbee, M., Suni, J., Blanco-Cano, X., Ganse, U., Pfau-Kempf, Y., Alho, M., Dubart, M., … Palmroth, M. (2021). Foreshock cavitons and spontaneous hot flow anomalies: a statistical study with a global hybrid-Vlasov simulation. *Ann. Geophys.*, *39*(5), 911–928. https://doi.org/10.5194/angeo-39-911-2021

Turc, L., Ganse, U., Pfau-Kempf, Y., Hoilijoki, S., Battarbee, M., Juusola, L., Jarvinen, R., Brito, T., Grandin, M., and Palmroth, M. (2018). Foreshock properties at typical and enhanced interplanetary magnetic field strengths: results from hybrid-Vlasov simulations. *J. Geophys. Res.: Space Phys.*, *123*(7), 5476–5493. https://doi.org/10.1029/2018JA025466

von Alfthan, S., Pokhotelov, D., Kempf, Y., Hoilijoki, S., Honkonen, I., Sandroos, A., and Palmroth, M. (2014). Vlasiator: first global hybrid-Vlasov simulations of Earth's foreshock and magnetosheath. *J. Atmos. Solar-Terr. Phys.*, *120*, 24–35. https://doi.org/10.1016/j.jastp.2014.08.012

Walsh, B. M., Komar, C. M., and Pfau-Kempf, Y. (2017). Spacecraft measurements constraining the spatial extent of a magnetopause reconnection X line. *Geophys. Res. Lett.*, 44(7), 3038–3046. https://doi.org/10.1002/2017GL073379

Wang, C., and Sun, T. R. (2022). Methods to derive the magnetopause from soft X-ray images by the SMILE mission. *Geosci. Lett.*, 9(1), 30. https://doi.org/10.1186/s40562-022-00240-z

Wang, Y. L., Elphic, R. C., Lavraud, B., Taylor, M. G. G. T., Birn, J., Raeder, J., Russell, C. T., Kawano, H., Zong, Q. G., … Friedel, R. H. (2005). Initial results of high-latitude magnetopause and low-latitude flank flux transfer events from 3 years of Cluster observations. *J. Geophys. Res.: Space Phys.*, 110(A11), A11221.

https://doi.org/10.1029/2005JA011150

Zhang, H., Kivelson, M. G., Khurana, K. K., McFadden, J., Walker, R. J., Angelopoulos, V., Weygand, J. M., Phan, T., Larson, D., … Auster, H. U. (2010). Evidence that crater flux transfer events are initial stages of typical flux transfer events. *J. Geophys. Res.: Space Phys.*, 115(A8), A08229. https://doi.org/10.1029/2009JA015013

Zhang, Y. J., Sun, T. R., Wang, C., Ji, L., Carter, J. A., Sembay, S., Koutroumpa, D., Liu, Y. D., Liang, G. Y., … Zhao, X. W. (2022). Solar wind charge exchange soft X-ray emissions in the magnetosphere during an interplanetary coronal mass ejection compared to its driven sheath. *Astrophys. J. Lett.*, 932(1), L1. https://doi.org/10.3847/2041-8213/ac7521

Supplementary material for "Hybrid-Vlasov simulation of soft X-ray emissions at the Earth's dayside magnetospheric boundaries"

The Supplementary Material consists of one Figure S1 and three movies S1–S3, whose descriptions are given below.
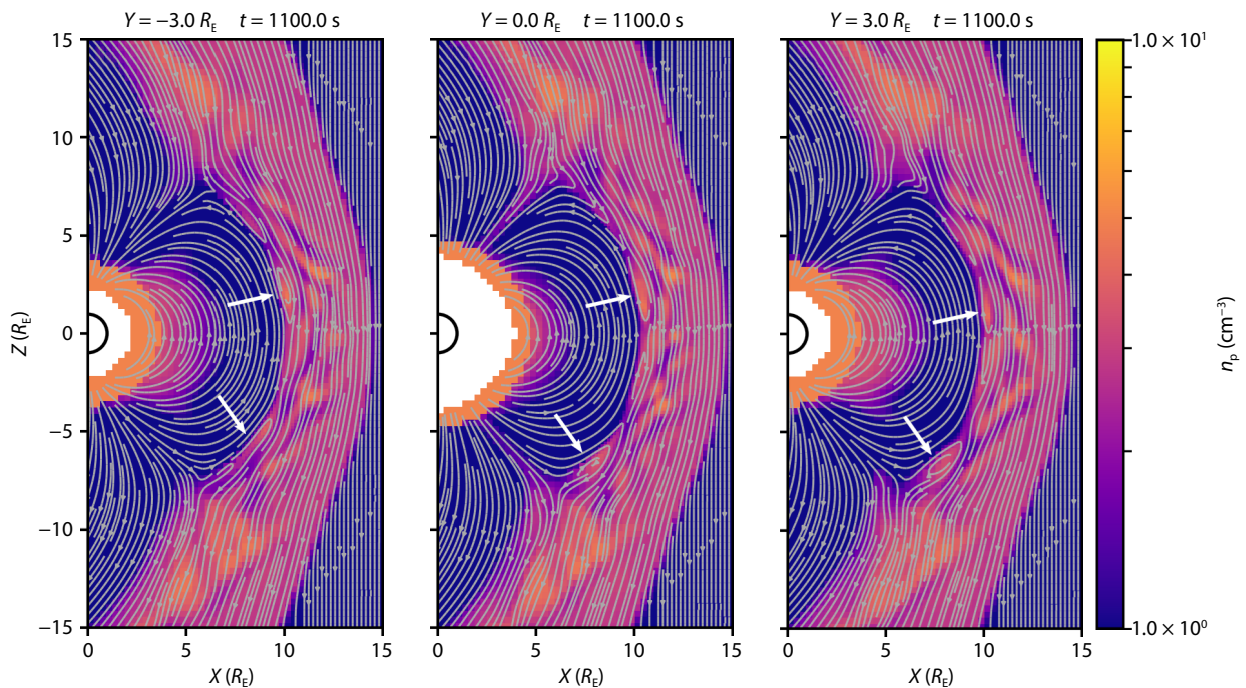

Figure S1. Proton density at $t = 1100$ s in three planes: (a) $Y = -3 R_E$, (b) $Y = 0$, and (c) $Y = 3 R_E$. The grey streamlines denote the in-plane magnetic field. White arrows indicate FTEs, which exhibit proton density enhancements in their core and show as magnetic islands. One can see that two FTEs are present and extend over at least 6 Earth radii along the Y direction.

Captions for Movies S1–S3

Movie S1. Animation of Figure 2 from $t = 800$ to $t = 1506$ s. (a) Proton number density, (b) proton bulk velocity, and (c) local soft X-ray emissivity in the $Y = 0$ plane. (d) Instantaneous soft X-ray image with 1 s integration time from a virtual spacecraft placed at $(0, -30 R_E, 0)$. The red trapezoid in panel (c) indicates the intersection of the instrument's field of view shown in panel (d) with the $Y = 0$ plane.

Movie S2. Animation of Figure 3 from $t = 800$ to $t = 1506$ s. (a) Proton number density, (b) proton bulk velocity, and (c) local soft X-ray emissivity in the $Z = 0$ plane. (d) Instantaneous soft X-ray image with 1 s integration time from a virtual spacecraft placed at $(0, 0, 30 R_E)$. The red trapezoid in panel (c) indicates the intersection of the instrument's field of view shown in panel (d) with the $Z = 0$ plane.
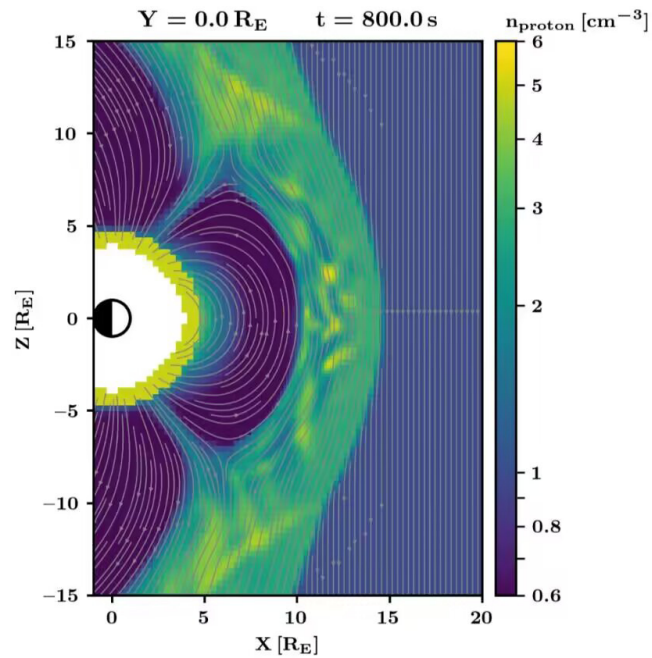
Movie S3. Proton number density in the $Y = 0$ plane from $t = 800$ to $t = 1506$ s. Grey lines indicate magnetic field lines. Flux transfer events can be identified as regions of increased proton density within magnetic islands and propagating toward higher latitudes along the dayside magnetopause. Mirror-mode waves can be seen as Earthward-propagating structures with oblique orientation in the magnetosheath.

Grandin M et al.: Vlasiator simulation of solar wind charge exchange soft X-ray emissions